Metallogenic model of the Lykling ophiolite-hosted lode Au deposit, Scandinavian Caledonides: Insight from fluid inclusions, mineral chemistry and stable isotope geochemistry

Sabina Strmić Palinkaš [a,b,*], Frida Riple Forsberg [b,c], Rolf Birger Pedersen [b], Håvard Hallås Stubseid [b], Seán H. McClenaghan [d], Jorge E. Spangenberg [e]

[a] *UiT The Arctic University of Norway, Faculty of Sciences and Technology, Department of Geosciences, Dramsvegen 201, N-9037 Tromsø, Norway*
[b] *University of Bergen, Faculty of Mathematics and Natural Sciences, Department of Earth Science, Centre for Deep Sea Research, Allegaten 41, 5007 Bergen, Norway*
[c] *Geological Survey of Norway, Leiv Eirikssons vei 39, N-7491 Trondheim, Norway*
[d] *Trinity College Dublin, School of Natural Sciences, Department of Geology, College Green, Dublin 2, Ireland*
[e] *University of Lausanne, Institute of Earth Surface Dynamics, Geopolis, CH-1015 Lausanne, Switzerland*

A B S T R A C T

The Lykling lode Au deposit represents a unique example of gold mineralization in the Upper Allochthone of the Scandinavian Caledonides. The mineralization is hosted by the Early Ordovician Lykling Ophiolite Complex and the intruding trondhjemite unit and spatially associated with two generations of mafic dykes that crosscut both the ophiolitic complex and trondhjemite. Field observations indicate that the mafic dykes did not play an active role in the emplacement of Au at Lykling, however their contacts with the immediate host rocks (i.e., gabbro and trondhjemite) may have focused ore-forming fluids.

Three main stages in the evolution of the hydrothermal system in the Lykling area are documented by two generations of auriferous quartz veins: 1) older quartz-carbonate veins hosted by moderately angled brittle-ductile shear zones and 2) younger quartz-sulfide veins that fill steeply dipping brittle faults. Stage 1 resulted in deposition of barren quartz and gold-free pyrite from moderately saline $NaCl\text{-}CaCl_2\text{-}H_2O \pm CO_2$ fluids at temperatures between ~310–330 °C and pressures in the range from 2.7 to 3.5 kbars. Under the given physicochemical conditions Au was mobile in the form of its chloride complexes. Stage 2 is associated with multiple episodes of ductile deformation punctuated by concomitant brecciation reflecting brittle-ductile transition processes. Fluid inclusion data reveals a decrease in temperature and pressure that may result in the formation of stable Au-bisulfide complexes and making the hydrothermal mobility of Au sensitive to changes in pressure. Consequently, the fluctuation in pressure controlled by the development of brittle-ductile structures likely resulted in the precipitation of native gold in quartz veins. Stage 3 represents a pure brittle event which is accompanied by a significant decrease in the fCO_2/fS_2 ratio. Mixing of higher-temperature and moderate-salinity fluids with cooler fluids has been recognized as the principal trigger for deposition of sulfides and a paragenetically late phase of native gold in the Lykling hydrothermal system.

The Lykling ophiolite-hosted lode Au deposit shows numerous similarities with orogenic gold deposits elsewhere, including structural controls during mineralizing events, deposition from moderately to low salinity CO_2-bearing aqueous solutions, deposition from a focused fluid flow along *trans*-crustal fault zones with a mixed brittle-ductile character and the spatial association with regionally metamorphosed terranes. In contrast to the great majority of the known orogenic gold deposits, the Lykling ophiolite-hosted lode Au deposit records a magmatic origin of volatiles. Therefore, taking into consideration field relationships and the regional setting of the Lykling deposit, we argue that its formation is concomitant with emplacement of the Sunnhordland Batholith during post-collisional thinning of the crust and associated localized uplift within the Lykling Ophiolite Complex.

1. Introduction

Lode-type gold mineralization is characterized by structurally controlled quartz-carbonate-sulfide veins typically deposited from low-salinity H_2O–CO_2 fluids at crustal depths between 2 and 15 km (e.g., Groves et al., 1998; Bierlein & Crowe, 2000; Gaboury, 2019; Groves et al., 2020; Goldfarb & Pitcairn, 2023). The mineralization often records the deposition from a focused fluid flow along *trans*-crustal structures of mixed brittle-ductile character (Goldfarb et al., 2005; Tavares Nassif et al., 2022). The lode gold deposits have been found in regionally metamorphosed terranes of all ages and their host rocks usually reflect conditions of upper greenschist to amphibolite-facies metamorphism (Goldfarb et al., 2005). Pre-metamorphic protoliths hosting the Archaean lode gold deposits are predominantly volcanic and plutonic lithologies formed in an oceanic back-arc setting. In contrast, younger deposits are usually associated with terranes mainly composed
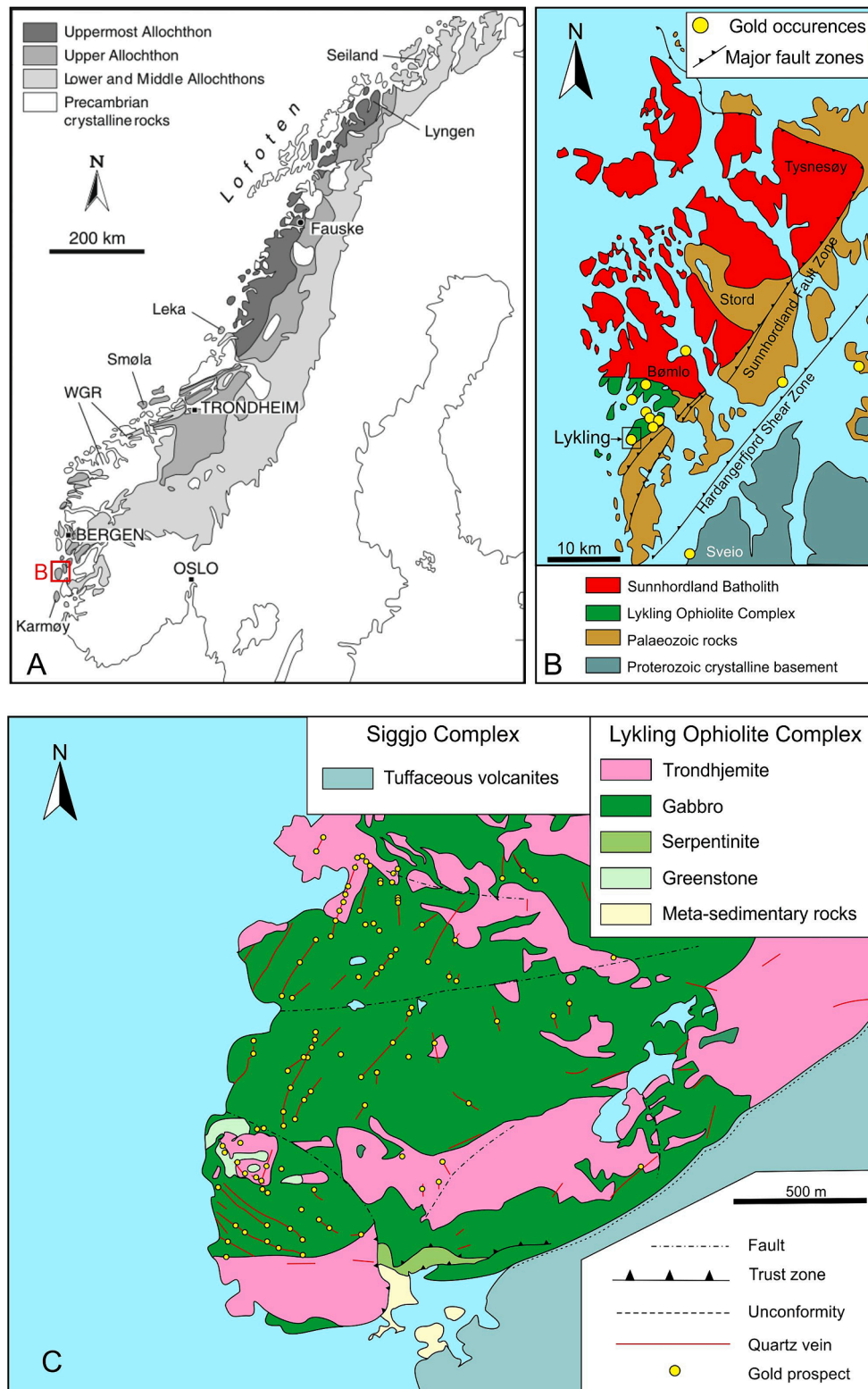
Fig. 1. A) Simplified geological map of the Scandinavian Caledonides (after Roberts, 2003) with marked position of the most prominent ophiolite complexes; B) Geological map of the Bømlo island, NW Norway, with the study area marked; C) Geological map of the Lykling area (after Grenne et al., 1999).

of clastic marine sediments (Groves et al., 1998; Bierlein & Crowe, 2000). Ophiolite-hosted lode gold deposits have been so far mostly studied in the Neoproterozoic greenstone belts of the Nubian Shield, Egypt (e.g., Botros, 2002; Zoheir, 2011, Zoheir et al., 2019a). Numerous studies suggest that devolatization of country rocks during orogeny-driven metamorphic events played a key role in generation of gold-bearing fluids (e.g., Goldfarb et al., 2005; Groves et al., 2020; Patten et al., 2020; Stepanov, 2021). Anyhow, in some deposits a substantial contribution of magmatic fluids cannot be excluded (e.g. Doublier et al., 2014; Kerr et al., 2018; Fabricio-Silva et al., 2021; Wu et al., 2021).

The Scandinavian Caledonides, an orogenic belt extending for about 1500 km from the Stavanger region in southern Norway to the Barents
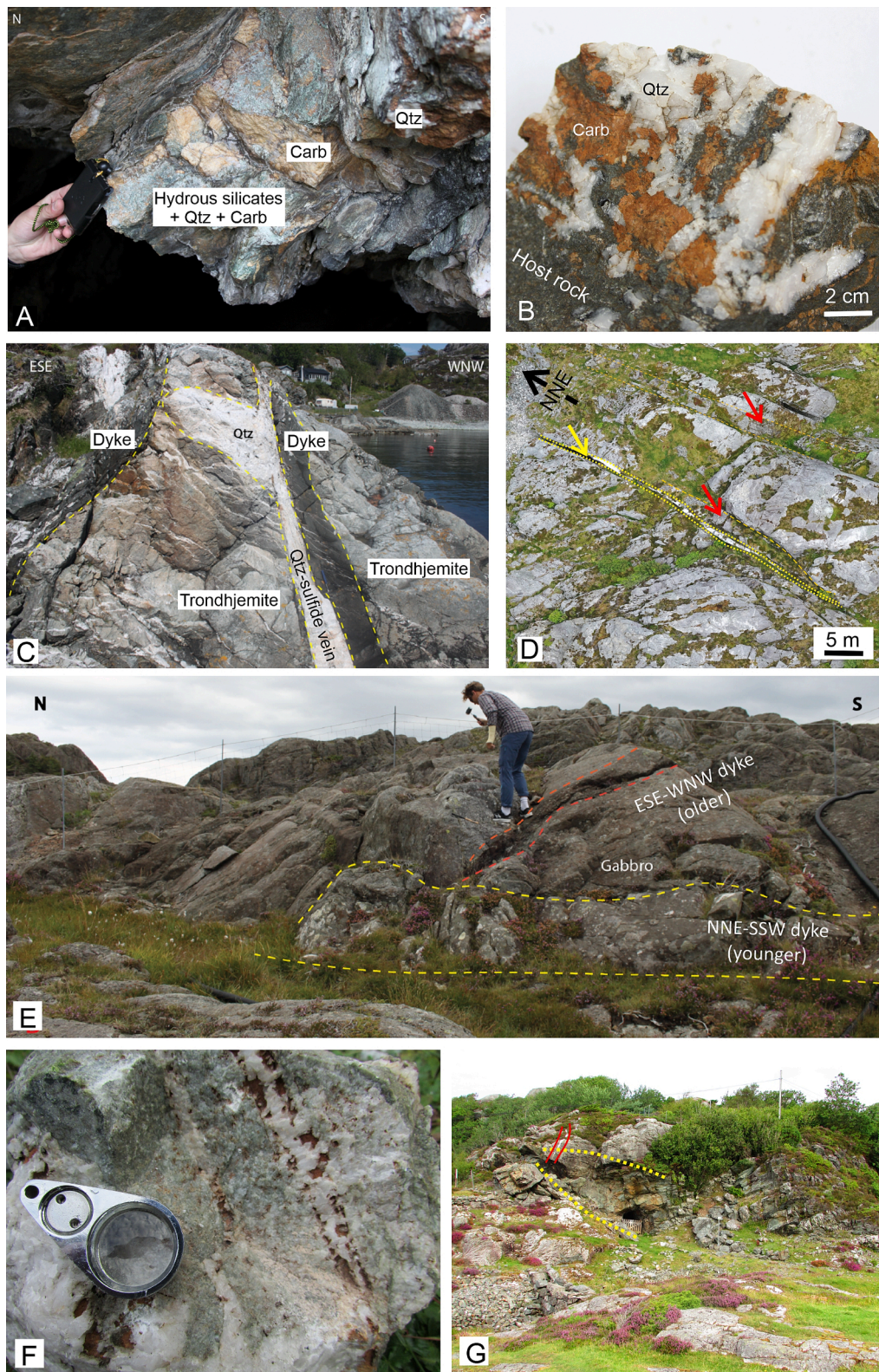
Fig. 2. **A)** A mineralized brittle-ductile shear zone. A quartz-carbonate vein is embedded within a hydrothermal alteration halo composed of the mixture of hydrous silicates, mostly chlorites, quartz and carbonates; **B)** A hand specimen of a quartz-carbonate vein associated with the hydrothermally altered mafic dyke; **C)** A mineralized quartz-sulfide vein hosted by a brittle fault spatially associated with a NNE-SSW oriented mafic dike that intruded trondhjemite; **D)** An overview of a mineralized quartz-sulfide vein (yellow arrow) hosted by a brittle fault spatially associated with a set of NNE-SSW oriented mafic dykes (red arrow) hosted by trondhjemite (the photo taken by a drone); **E)** The Lykling Ophiolite gabbro intruded by two generations of mafic dykes. The younger NNE-SSW dyke (yellow dots) cut the older ESE-WNW oriented dyke (red dots); **F)** A hand specimen of a quartz-sulfide vein showing an open space texture; **G)** A mineralized ductile–brittle shear zone (yellow lines) cut by a mineralized brittle quartz vein (red lines) reflects relative timing of emplacement of these two types of the Au mineralization. Abbreviations: Qtz-Quartz; Carb-Carbonate. (For interpretation of the references to colour in this figure legend, the reader is referred to the web version of this article.)
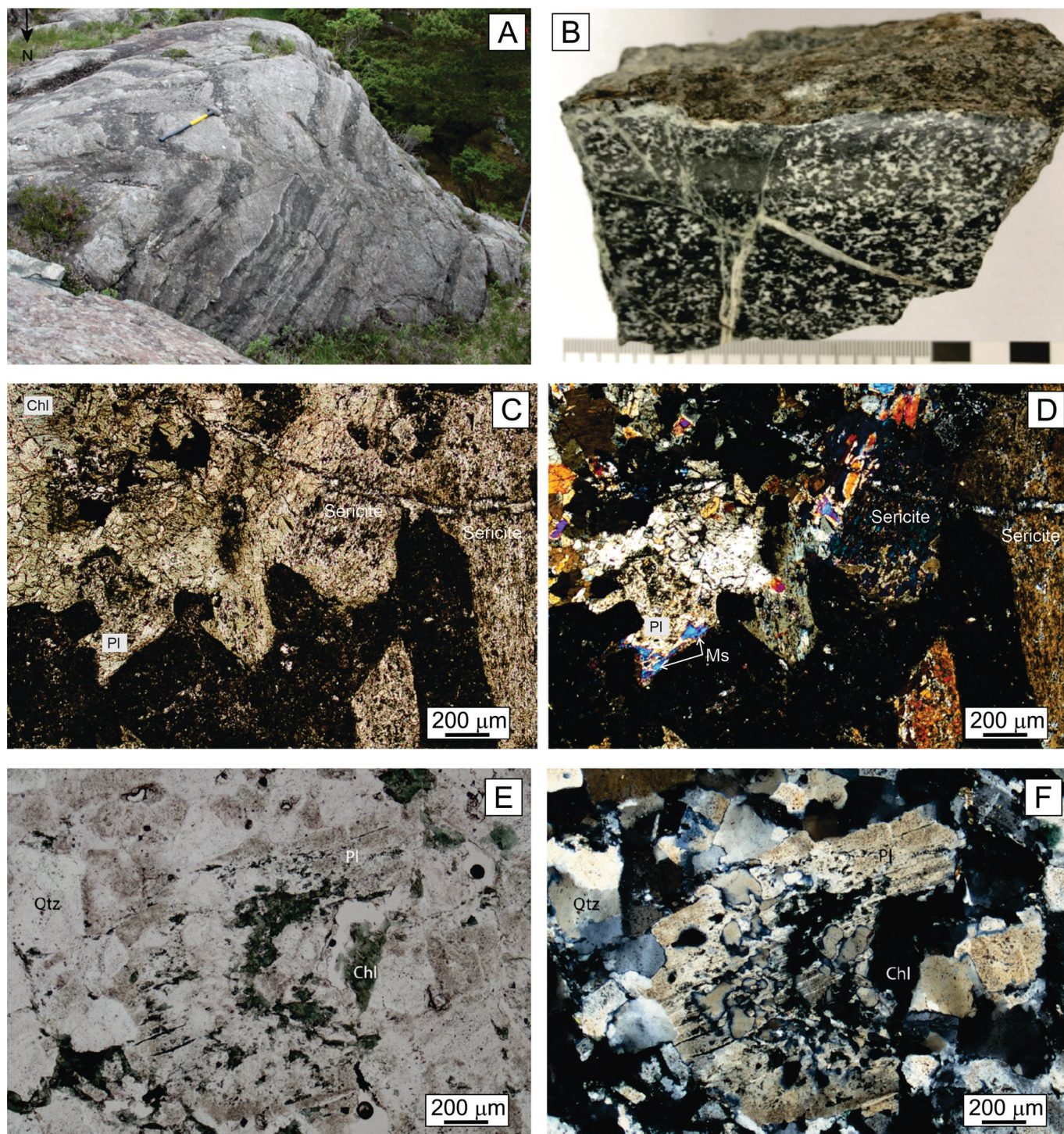
Fig. 3. A) The layered variety of the Lykling Ophiolite gabbro. It is characterized by a rhythmic alternation of melanocratic and leucocratic layers with their thickness from few centimetres up to several meters; **B)** A hand specimen of the massive variety of the Lykling Ophiolite gabbro; **C)** Photomicrograph of hydrothermally altered gabbro, PPL; **D)** Photomicrograph of hydrothermally altered gabbro, XPL; **E)** Photomicrograph of hydrothermally altered trondhjemite showing abundant chlorite, PPL; **F)** Photomicrograph of hydrothermally altered trondhjemite showing saussurization of plagioclase, XPL. Abbreviations: Chl-Chlorite; Qtz-Quartz; Pl-Plagioclase.

Sea region in northern Norway (Fig. 1A), host several ophiolite terranes that represent remains of the late Neoproterozoic to early Palaeozoic Iapetus Ocean realm (e.g., Dunning & Pedersen, 1988; Pedersen & Furnes, 1991; Corfu et al., 2014). The main type of mineralization found in these terranes belongs to syngenetic volcanogenic massive sulfide (VMS) deposits (e.g., Grenne et al., 1999) but the Lykling ophiolite in SW Norway (Fig. 1B) represents an exception because, in addition to VMS

mineralization (Strmić Palinkaš et al., 2024), it also hosts numerous epigenetic lode-type gold occurrences.

The Lykling ophiolite-hosted Au mineralization occurs in two types of structurally controlled hydrothermal veins: 1) older quartz-carbonate veins hosted by moderately inclined brittle-ductile shear zones, and 2) younger sulfide-rich quartz veins hosted by steeply dipping brittle faults. The mineralization is spatially associated with two generation of mafic

Table 1

Major element composition of the barren Lykling Ophiolite gabbro and trondhjemite and mafic dykes from the Lykling area, SW Norway.

Sample ID	Lithology	Associated mineralization	Na$_2$O	MgO	Al$_2$O$_3$	SiO$_2$	P$_2$O$_5$	K$_2$O	CaO	TiO$_2$	MnO	Fe$_2$O$_3$	LOI	Total
			wt,%											
20LYK20K	NNE-SSW oriented mafic dyke	Brittle quartz-sulfide vein	1.70	3.53	15.26	49.92	0.41	3.43	6.82	0.77	0.17	8.35	7.83	98.19
20LYK20L	NNE-SSW oriented mafic dyke	Brittle quartz-sulfide vein	2.92	1.93	16.57	54.06	0.27	3.98	5.46	0.51	0.11	5.23	6.30	97.34
19LYK2A	NNE-SSW oriented mafic dyke	Brittle quartz-sulfide vein	3.97	4.92	13.11	47.77	0.44	0.06	8.02	0.87	0.17	9.69	8.47	97.49
20LYK13B	ESE-WNW oriented mafic dyke	Brittle quartz-sulfide vein	1.75	8.22	11.99	36.78	0.07	0.07	6.35	2.53	0.22	26.91	3.72	98.61
20LYK38C	ESE-WNW oriented mafic dyke	Brittle quartz-sulfide vein	1.55	9.05	10.68	42.05	0.06	0.21	8.96	1.58	0.17	18.23	5.68	98.22
20LYK27E1	ESE-WNW oriented mafic dyke	Brittle-ductile shear zone, quartz-carbonate vein	0.78	8.43	12.27	44.20	0.07	1.74	7.28	0.47	0.21	9.38	13.95	98.78
20LYK12	NNE-SSW oriented mafic dyke	No mineralization associated	3.63	7.17	15.10	46.95	0.16	0.11	9.08	1.38	0.14	9.79	3.87	97.38
20LIND5	Massive gabbro, Lindøya	No mineralization associated	3.57	8.13	14.79	48.40	0.10	0.56	7.68	1.39	0.26	12.42	3.96	101.26
20ALS7B	Massive gabbro, Alsvågen	No mineralization associated	3.56	7.82	15.81	49.07	0.06	0.07	8.25	0.74	0.24	11.04	1.17	97.83
20LYK26C	Trondhjemite, Lykling	No mineralization associated	4.84	0.90	11.10	77.51	0.06	0.24	0.98	0.23	0.06	2.81	1.43	100.16

dykes that crosscut the Early Ordovician Lykling Ophiolite Complex and associated trondhjemite (Fig. 1C). Although the deposit is of a limited economic importance, it records ore-forming processes characteristic for the formation of ophiolite-hosted orogenic gold deposits.

The present contribution combines field observations with detailed mineralogical, trace element, stable isotope (δ^{13}C, δ^{18}O, δ^{34}S) and fluid inclusion studies of the Au mineralization and associated hydrothermal alteration products with an aim to establish a metallogenic model for the Lykling ophiolite-hosted gold deposit and to contribute to better understanding the lode-type gold mineralization overall.

2. Geological setting

2.1. Regional geology

The Scandinavian Caledonides represent a deeply eroded orogenic belt underlaid by the Fennoscandian shield (Corfu et al., 2014; Fig. 1A). The geological history of the Scandinavian Caledonides started about 850–900 Ma ago with incipient rifting and initiation of the Rodinia megacontinent break-up (Paulsson & Andréasson, 2002) followed by an advance rifting stage (730–800 Ma; Melezhik et al., 2015) and formation of the Iapetus Ocean (e.g., Grenne et al., 1999; Corfu et al., 2014; Gee, 2015). The contraction of the Iapetus Ocean in the late Cambrian was succeeded by an oblique collision and subduction of Baltica beneath Laurentia in the late Silurian to early Devonian (Roberts, 2003; Hacker & Gans, 2005; Slagstad & Kirkland, 2018). In Devonian times, the Scandinavian Caledonides were subjected to an orogenic collapse associated with widespread extension, basin development and sedimentation (Roberts, 2003). The sedimentary and volcano-sedimentary lithologies of the Uppermost Allochthon record a rifting environment along the Laurentian plate (e.g., Melezhik et al., 2015; Stephens, 2020), while shelf and continental rise successions indigenous to the Baltica plate have been preserved in Lower and Middle Allochthons (e.g., Roberts, 2003). The Upper Allochthon predominantly consists of Iapetus Ocean crust and remnants of several primitive and evolved magmatic arcs (e.g., Pedersen & Furnes, 1991; Pedersen et al., 1992; Grenne et al., 1999).

Ophiolite complexes can be found along the entire Upper Allochthone, from Karmøy in the south to Lyngen in the north (Fig. 1B; Dunning & Pedersen, 1988). They were formed during at least two episodes of spreading-related magmatism (e.g., Dunning & Pedersen 1988; Pedersen & Furnes, 1991). The older generation of ophiolites (early Ordovician) records a prolonged magmatic activity and shows a range of compositions from Mid-ocean ridge basalts (MORB), Island arc tholeiites (IAT), boninites and calc-alkaline to alkaline basalts. In contrast, the younger ophiolites (late Ordovician) are characterized by N- to E-MORB compositions. They are often associated with a melange composed of continentally-derived sediments, olistoliths of mature island arc-derived volcanics, clasts with a MORB-IAT affinity, cherts and sandstones (Pedersen & Furnes, 1991).

The ophiolitic terrains of SW Norway are represented by several dismembered ophiolite complexes well exposed along the coastline between Bergen and Stavanger. They cover an area of approximately 4000 km^2 with the Karmøy and Gullfjellet ophiolites as the largest and best-preserved complexes (Fig. 1A; Dunning and Pedersen 1988; Pedersen & Dunning, 1997). The Karmøy ophiolite complex is characterized by composite (polyphase) magmatic evolution that includes formation of an axis sequence from IAT- and MORB-like magmas (493 + 7/-4 Ma), intrusion of boninitic magmas (485 ± 2 Ma), intrusion of MORB- and IAT-like magmas, intrusion and extrusion of calc-alkaline magmas (470 + 9/-5 Ma), and intrusion and extrusion of basalts with alkaline trace-element affinity (Pedersen & Hertogen, 1990). The West Karmøy Igneous Complex (WKIC) intruded plutonic terrains within the ophiolite complex and crosscut the boninitic dyke swarms. WKIC consists of an outer quartz dioritic enclave that inwards alters to granodiorite and granite. The granite contains high amounts of sialic and amphibolitic xenoliths (Ledru, 1980). The Rb/Sr dating of WKIC yielded a relatively inaccurate age of about 479 ± 5 Ma (Pedersen & Dunning, 1997).

2.2. The Lykling ophiolite Complex

The Early Ordovician Lykling Complex is exposed on the islands of Bømlo and Stord (Fig. 1B). The complex consists of the Lykling ophiolite, the Geitung Unit, trondhjemite and the Søre Lyklingholmen Unit (Amaliksen & Sturt, 1986). The Lykling ophiolite records an almost complete ophiolitic sequence. An over 4 km thick gabbroic zone is composed of layered gabbro, homogeneous gabbro, microgabbro, gabbro pegmatite and diabase dykes that are succeeded by vesicular pillow basalts. The Geitung Unit is a volcano-sedimentary sequence that overlies the Lykling ophiolite. The volcanic sequence is composed of pillow lavas, *meta*-dacites and volcanic breccias and has an immature island arc trace element signature (Furnes et al., 1986). The overlying sedimentary sequence contains cherts, conglomerates and sandstones (Amaliksen & Sturt, 1986). The U-Pb age of zircons extracted from the volcanic portion of the Geitung Unit suggests a crystallization age of 494 ± 2 Ma (Pedersen & Dunning, 1997). The Lykling ophiolite and the

Table 2

Trace element composition of of the barren Lykling Ophiolite gabbro and trondhjemite and mafic dykes from the Lykling area, SW Norway.

Sample ID	Li	Sc	V	Cr	Co	Ni	Cu	Zn	Rb	Sr	Y	Zr	Nb	Cs	Ba	Hf	Ta	Pb	Th	U	Y
	ppm																				
20LYK20K	15.1	18.4	194.9	9.4	14.8	5.1	2.3	40.4	109.7	338.5	19.3	100.6	9.2	2.5	648.75	2.73	0.52	5.10	7.28	2.78	19.73
20LYK20L	10.8	8.3	98.3	1.0	9.8	0.7	67.6	40.3	152.2	430.9	19.2	112.6	9.8	3.4	870.40	2.92	0.58	6.96	8.69	3.03	18.95
19LYK2A	27.7	28.0	350.7	88.5	25.4	35.4	169.0	115.1	0.8	270.3	13.4	109.7	12.2	0.3	25.12	3.25	0.64	5.23	9.84	3.84	14.06
20LYK13B	19.7	63.7	1119.5	1.8	91.4	4.0	114.1	115.6	0.2	75.2	9.0	7.6	0.2	0.1	4.10	0.33	0.01	1.02	<0.0025	0.01	8.52
20LYK38C	13.5	74.6	932.6	190.4	78.0	51.6	145.3	70.3	5.6	117.5	10.4	9.0	0.1	0.8	32.46	0.40	0.02	4.89	<0.0025	0.01	10.52
20LYK27E1	34.0	30.3	197.1	579.9	27.3	162.1	59.4	139.7	41.3	78.3	15.6	24.5	0.3	0.6	112.60	0.82	0.03	11.29	0.20	0.12	15.97
20LYK12	22.1	31.5	216.8	343.9	37.8	35.4	21.8	70.7	1.2	143.2	21.7	97.7	7.8	0.1	17.31	2.72	0.53	0.87	1.99	0.41	21.76
20LIND5	12.5	39.8	337.6	113.5	41.0	35.8	46.7	107.0	8.1	238.9	24.8	49.4	2.0	0.5	132.40	1.54	0.15	3.54	0.30	0.12	24.42
20ALS7B	4.9	41.1	234.2	67.2	35.8	44.6	82.6	59.6	0.8	184.0	22.3	9.1	1.0	0.3	19.05	0.63	0.07	0.58	0.31	0.10	22.01
20LYK26C	4.9	11.3	6.1	1.0	1.7	0.9	16.2	26.5	4.6	49.3	34.8	27.6	1.7	0.2	45.57	1.27	0.11	1.99	0.51	0.30	33.71

Geitung Unit are intruded by voluminous amounts of trondhjemite (Nordås et al. 1985) and unconformably overlain by the Søre Lyklingholmen Unit. The U/Pb dating of trondhjemite yielded the age of 484 ± 6 Ma (Saltvedt, 2021). According to Amaliksen & Sturt (1986), the Søre Lyklingholmen Unit was formed in a tectonically active zone of the Iapetus Ocean floor.

The Lykling Complex is unconformably overlain by the Siggjo Complex (Fig. 1B), an approximately 1 km thick sequence of calc-alkaline subaerial basalt, andesites and rhyolites (Nordås et al. 1985). The U-Pb zircon dating gave an age of 473 ± 2 Ma (Pedersen & Dunning, 1997). The geochemical signature, with pronounced negative Ta and Nb anomalies, reflects a typical calc-alkaline island arc sequence.

The southernmost part of the Bømlo island is covered by the Langevåg Group. This formation consists of subaerial tuff-breccias, lavas, radiolarian chert, submarine volcaniclastic subaqueous debris flow, felspathic and tuffaceous turbidites and pillowed basalts deposited during a progressive deepening of the back-arc basin (Brekke et al. 1984).

The Sunnhordland Batholith (Fig. 1B) covers an area of approximately 1000 km^2. It is composed of calc-alkaline plutons ranging in the composition from gabbroic to granitic (Andersen & Jansen, 1987). The U-Pb dating of its oldest sections yielded an age of 472 ± 2 Ma (Pedersen & Dunning, 1997). The batholith was emplaced in a package of ophiolite and island-arc complexes, as well as sediments and volcanites of early Ordovician age that were developed in a zone of plate convergence (Andersen et al., 1991; Slagstad et al., 2011; Fossen et al., 2024).

The Hardangerfjord Shear Zone (Fig. 1B) is a NE–SW-trending low-angle extensional structure that extends for more than 600 km and shows displacement of up to 10–15 km (Fossen & Hurich, 2005). Deep seismic data indicate that the ductile shear zone continues down to the lower crust (20–25 km) at a dip of 22–23, where it appears to flatten and merge with the general lower-crustal deformation fabric. Onshore, the Hardangerfjord Shear Zone consists of a system of hard-linked ductile shear-zone segments (Fossen & Hurich, 2005). The Hardangerfjord Shear Zone separates the Precambrian basement from the Caledonian nappes and is considered to be a product of post-collisional processes that affected the Scandinavian Caledonides during the Devonian (Fossen & Dunlap, 1998; Fossen, 2000; Fossen & Hurich, 2005; Fossen et al, 2017).

2.3. The Lykling ophiolite-hosted Au mineralization

Gold in the Lykling area was discovered in 1862 and the most of mining activities in the area happened between 1882 and 1910. In that period, the Oscar Gold Mining Company extraxted 157 kg of Au from about 63,000 t of mineralized rocks. The average ore grade has been estimated to ~ 2.5 g/t Au (Wulff & Stendal, 1995). The gold-bearing mineralization is hosted by the Lykling ophiolite gabbro and the intruding trondhjemite (Fig. 1C). The mineralization occurs in the form of quartz veins hosted by brittle-ductile shear zones (Fig. 2A and 2B) and brittle faults (Fig. 2C and 2D). In total, 14 quartz veins have been documented in the study area. Both types of veins are spatially associated with two sets of mafic dykes that crosscut the both the Lykling Ophiolite Complex and the intruding trondhjemite (Fig. 1C). The older generation of the dykes strikes in an ESE-WNW orientation and shows a tholeiitic character, while the younger generation has a NNE-SSW orientation and a calc-alkaline character (Fig. 2E; Amaliksen, 1983).

The mineralized shear zones are moderately angled (30-50°) and show a sigmoidal geometry indicative for ductile deformations. They host quartz-carbonate veins. Ankerite has been recognized as the main carbonate mineral. This type of veins contains only minor amounts of pyrite. Other sulfides are absent (Fig. 2A). The mineralized shear zones are enveloped by a hydrothermal alteration halo predominantly characterized by intermingling of quartz pods with masses of carbonates and hydrous silicate minerals, mostly chlorite and minor amounts of mica. Field observations and textural characteristics indicate that the shear

Table 3
Rare Earth Element (REE) content of of the barren Lykling Ophiolite gabbro and trondhjemite and mafic dykes from the Lykling area, SW Norway.

Sample ID	La	Ce	Pr	Nd	Sm	Eu	Gd	Tb	Dy	Ho	Er	Tm	Yb	Lu
	ppm													
20LYK20K	28.070	56.020	7.050	29.180	5.880	1.650	5.000	0.714	4.000	0.771	2.210	0.309	2.010	0.301
20LYK20L	32.530	63.090	7.630	30.880	5.800	1.580	4.730	0.696	3.970	0.791	2.250	0.316	2.110	0.335
19LYK2A	19.740	45.460	6.250	26.810	5.140	1.290	4.090	0.553	2.980	0.592	1.710	0.240	1.600	0.256
20LYK13B	0.368	1.100	0.210	1.540	0.696	0.439	1.220	0.234	1.700	0.379	1.100	0.162	1.080	0.166
20LYK38C	0.370	1.380	0.278	2.080	0.964	0.384	1.490	0.287	2.040	0.440	1.240	0.177	1.130	0.169
20LYK27E1	2.540	5.810	0.928	5.270	1.820	0.659	2.590	0.421	2.650	0.566	1.640	0.230	1.460	0.231
20LYK12	12.100	25.920	3.600	16.160	4.040	1.400	4.510	0.754	4.640	0.928	2.590	0.361	2.280	0.337
20LIND5	3.950	10.590	1.780	9.450	3.110	1.090	4.180	0.718	4.750	1.010	2.910	0.423	2.640	0.389
20ALS7B	2.710	8.390	1.510	8.310	2.720	0.967	3.500	0.623	4.090	0.901	2.650	0.393	2.540	0.389
20LYK26C	3.690	10.160	1.720	9.410	3.400	0.832	4.930	0.946	6.550	1.420	4.220	0.648	4.260	0.648

zones in the study area have been reworked through multiple episodes of ductile deformations and brecciations. In contrast, the quartz veins that occur along steeply dipping brittle faults (75-90°). This type of veins does not contain carbonates, but carry significant amounts of sulfides, predominantly pyrite and chalcopyrite. The quartz-sulfide vein assemblage is characterized by open-space filling textures (Fig. 2F). Transitions from the veins towards the host rocks are usually sharp, with only locally developed minor amounts of hydrothermal alterations. The thickness of the veins varies from several tens of cm up to 2 m. Field relationships suggest that the brittle quartz veins overprint the brittle-ductile shear zones (Fig. 2G).

3. Samples and methods

3.1. Samples

In total, 41 samples were collected from the Lykling ophiolite-hosted Au mineralization (Appendix 1), including 13 samples of quartz-carbonate veins, 14 samples of quartz-sulfide veins, 10 samples of mafic dykes (three of the ESE-WNW orientation dykes and seven with the NNE-SSW orientation), one sample of the host gabbro and three trondhjemite samples. Representative samples were prepared as polished thin and thick sections suitable for petrographic and microanalysis. Samples selected for fluid inclusion studies were prepared as 0.1 mm to 0.3 mm thick double polished wafers. Samples of host rock and mafic dykes selected for lithogeochemical and X-ray diffraction (XRD) analyses were pulverized in an agate mill. Mineral grains selected for stable isotope analyses were micro-drilled.

3.2. Analytical methods

Petrographic studies were conducted on polished thin and thick sections using transmitted and reflected light microscopy. The textural features and semi-quantitative analyses of mineralized samples were examined on carbon-coated polished sections using a Zeiss supra 55VP Scanning Electron Microscope (SEM) equipped with an Energy-Dispersive X-ray (EDX) spectrometer at the University of Bergen. EDX analyses were conducted with a Thermo Noran detector at a working distance of 8.5 mm, using an accelerating voltage of 20 kV and an aperture of 60 μm.

A quantitative analysis of chlorite was carried out using a Zeiss Merlin Compact VP field emission SEM equipped with an EDX spectrometer at UiT The Arctic University of Norway. EDX analyses were conducted with an X-Max80 EDX detector by Oxford instruments at a working distance of 8.5 mm, using an accelerating voltage of 20 kV and an aperture of 60 μm. The retrieved data were further processed by applying the AZTec software provided by Oxford instruments.

XRD analysis was conducted at the University of Bergen, Norway, using a D8 ADVANCE ECO X-Ray diffractometer (45 kV, 40 μA) with CuKα-monochromatized radiation (λ = 1.54056 Å) and θ-θ geometry. The area between 4 and 90° 2θ, with 0.02° steps, was measured with a

0.5° primary beam divergence. Compound identifications were based on the reference database DIFFRAC.EVA.

Lithogeochemical analyses were performed at the University of Bergen combing X-Ray Fluorescence (XRF) spectroscopy, Inductively Coupled Plasma Mass Spectrometry (ICP-MS) and Inductively Coupled Plasma Atomic Emission Spectrometer (ICP-AES) techniques. The XRF analysis was applied to obtain the total silica content. Fused glass disks with lithium teatraborate were analyzed using an AXS S4 Pioneer XRF. The analytical precision better than ± 0.01 wt% was estimated from replicate analyses of GSP-1 (Silver Plume Granodiorite) and BCR-2 (Colombia River Basalt) standards. The other major elements as well as a range of trace elements were measured from solutions prepared by an HF-HNO$_3$-HCl digestion of pulverized rock samples. A Thermo Scientific ICap 7600 Inductively Coupled Plasma Atomic Emission Spectrometer (ICP-AES) was used to determine the major and trace element concentrations, except REE. The REE concentrations were analyzed using a Thermo Scientific Element XR^{TM} Inductively Coupled Plasma Mass Spectrometer (ICP-MS). The BCR-2 standard was used for both ICP-AES and ICP-MS analyses.

The ore grade was determined at Bureau Veritas Minerals, Canada. The Fire Assay Au method (code FA330-Au) was suitable for samples with the Au content between 2 ppb and 10 ppm. Samples with the content >10 ppm were also analyzed by a gravimetric method (code FA530-Au).

Laser Ablation ICP-MS spot analysis and high-resolution trace element mapping of sulphide phases were performed at the Raw Materials Characterization Laboratory at Trinity Collage Dublin, Ireland. A Teledyne PhotonMachines G2 193 nm Excimer ArF laser with a HelEx II 2- vol cell coupled to a Thermo Elemental iCapQs ICP-MS was used to carry out in situ mineral analyses on thin sections. Sulfide phases were analysed for ^{34}S, ^{57}Fe, ^{59}Co, ^{60}Ni, ^{65}Cu, ^{66}Zn, ^{75}As, ^{77}Se, ^{92}Mo, ^{109}Ag, ^{117}Sn, ^{121}Sb, ^{125}Te, ^{197}Au, ^{202}Hg, ^{207}Pb, and ^{209}Bi. Isotopes were selected to avoid significant isobaric-mass and polyatomic-molecular interferences; mass spectrometer dwell times were set to 0.02 s for most elements except for Co (0.04 sec), Ni (0.04), As (0.05), Se (0.04), Sb (0.04), Te (0.05) and Au (0.06). Trace element mapping of mineralization was carried out by ablating lines with a 10 μm beam diameter with a 1 μm overlap. proceeding as a continuous profile at 12 μm/sec with a repetition rate of 20 Hz and a fluence of 1.10 J/cm^2; all other parameters were kept constant. For the spot analyses, a spot size of 20 μm (square) was used, with a repetition rate of 6 Hz over 30 s and a fluence of 1.20 J/cm^2. Data were calibrated using a MASS-1 (Wilson et al, 2002) sulphide standard with UQAC FeS-1 (Savard et al., 2018) analysed as a secondary standard. A fully quantitative data reduction was performed in Iolite applying the internal standardization method of Ulrich et al. (2009); internal standards of Fe and Cu were applied in the reduction of data for pyrite and chalcopyrite, respectively. Concentration data were obtained by applying the data reduction scheme 'Trace-Elements' (Woodhead et al, 2007) in 'Internal Element Standard mode.

Petrographic and microthermometric analyses of fluid inclusions within transparent quartz associated with the ore mineralization were
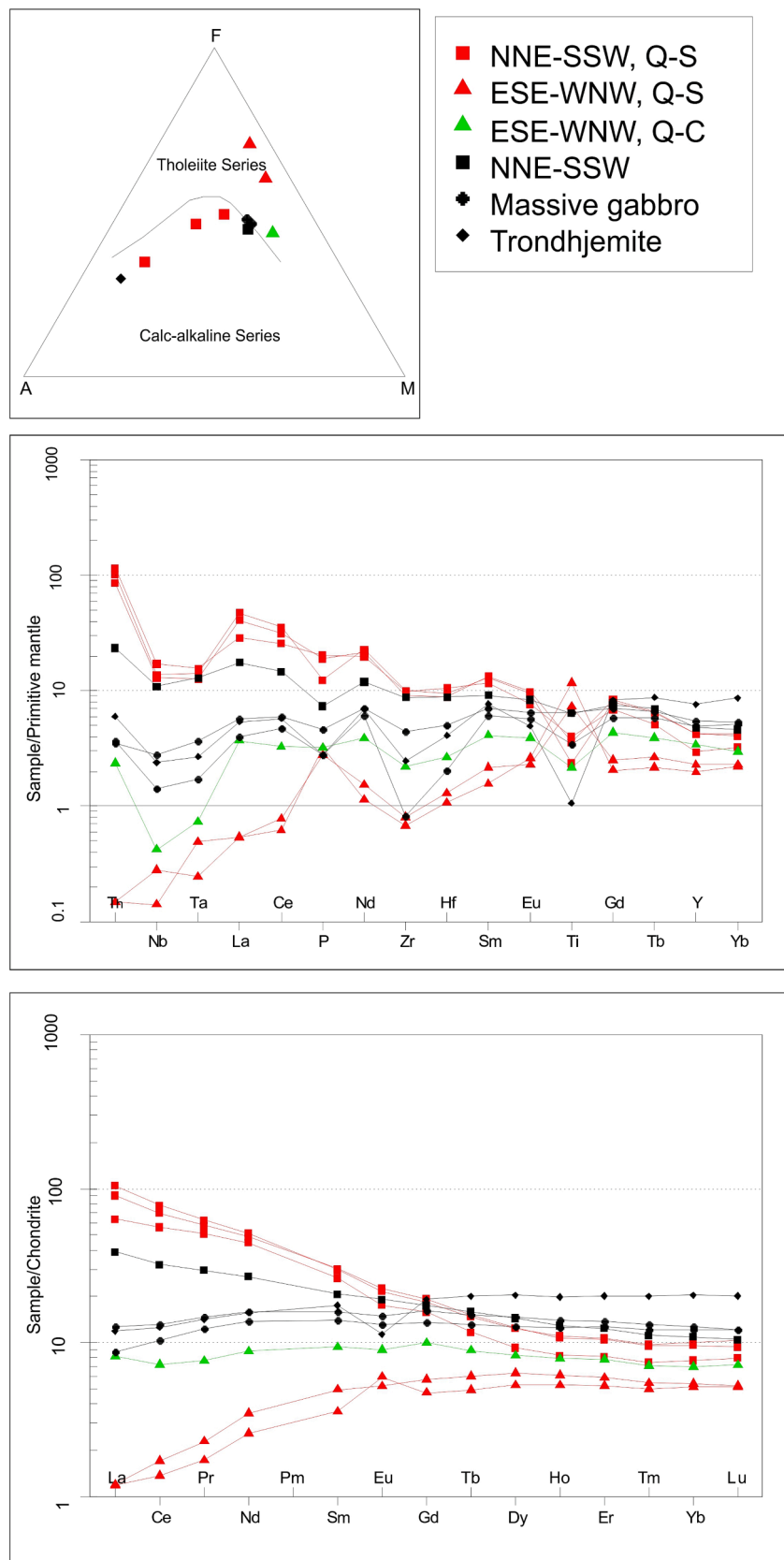
Fig. 4. Lithogeochemical data obtained from the barren Lykling Ophiolite gabbro and trondhjemite and mafic dykes associated with the quartz-carbonate veins (Q-C) and the quartz-sulfide veins (Q-S) in the Lykling area; **A)** AFM diagram (after Irvine and Baragar, 1971)**; B)** Primitive mantle normalized incompatible element spider diagram (after Sun & McDonough, 1989)**; C)** Chondrite normalized plots of REE concentrations (after Boynton, 1984).
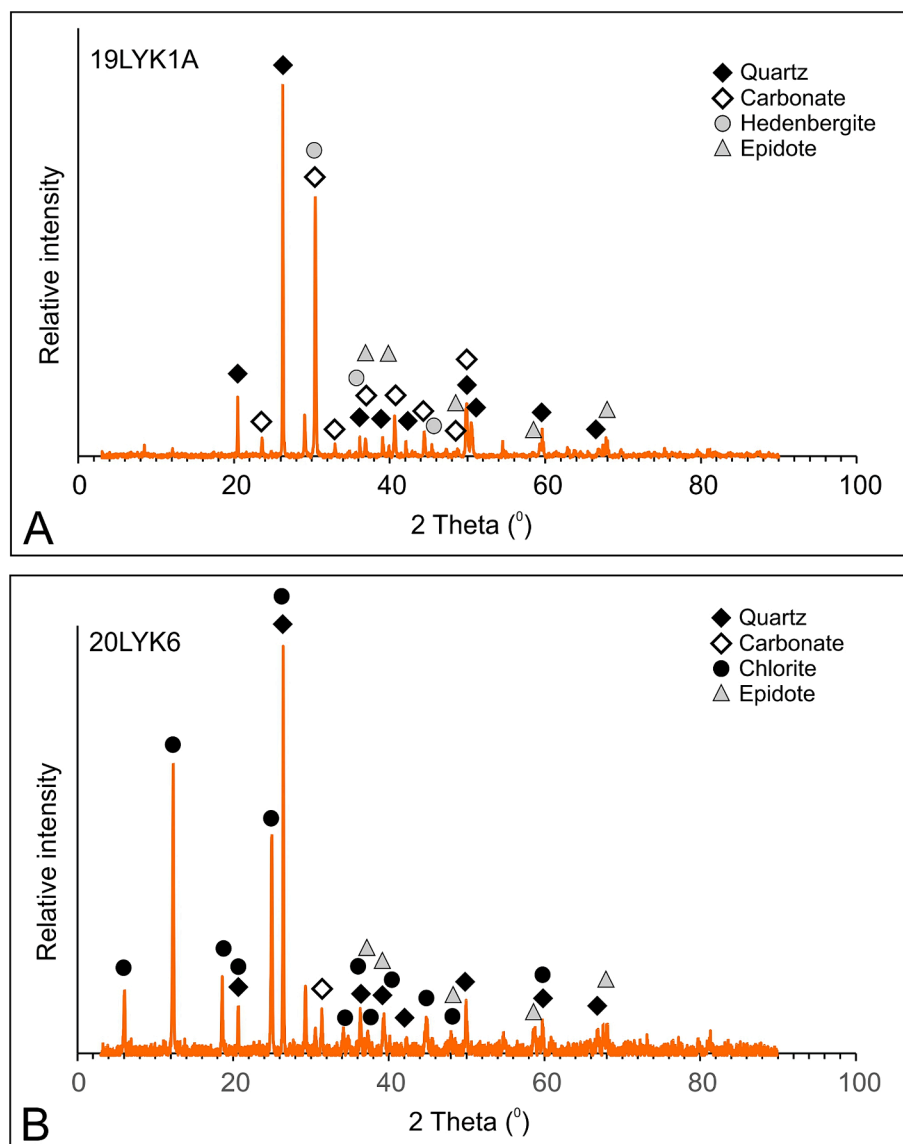
Fig. 5. XRD patterns obtained from **A)** A typical hydrothermal alteration assemblage associated with mineralized brittle-ductile shear zones (sample 19LYK1A); **B)** A typical hydrothermal alteration assemblage associated with emplacement of mineralized brittle quartz-sulfide veins into the mafic dykes (sample 20LYK6).

performed at UiT The Arctic University of Norway. Double polished, 0.1 mm to 0.3 mm thick, translucent mineral wafers were studied. For the temperature range between −180 and + 600 °C, measurements were carried out on a Linkam THMS 600 stage while higher homogenization temperatures were recorded using a Linkam TS1400XY stage. Both stages were mounted on an Olympus BX 2 using 10 × and 50 × Olympus long-working distance objectives. Two synthetic fluid inclusion standards (SYN FLINC; pure H_2O and mixed H_2O–CO_2) were used to calibrate the equipment. The precision of the system was ± 2.0 °C for homogenization temperatures and ± 0.2 °C in the temperature range between − 60° and + 10 °C. Microthermometric measurements were conducted on defined fluid inclusion assemblages (FIAs), representing groups of inclusions that were trapped simultaneously. The FIAs were identified based on petrographic analysis before heating and freezing (Goldstein, 2001; Bodnar, 2003). During microthermometric measurements, the following phase transitions were recorded: the first-melting temperature (eutectic T_e), the last melting temperature of ice ($T_{m\ ice}$), and the total homogenization temperature (T_H). Calculations of compositions, densities, and isochores were conducted applying the numerical model by Steele-MacInnis (2018) for the H_2O-NaCl-CO_2 system and Steele-MacInnis et al. (2012) for the H_2O-NaCl system.

Carbon and oxygen isotope analyses of carbonates were performed at the University of Lausanne, Switzerland, using a Thermo Fisher (Bremen, Germany) carbonate preparation device and Gas Bench II connected to a Delta V Plus isotope ratio mass spectrometer (Révész & Landwehr, 2002). The CO_2 extraction was performed by reacting 200–250 μg sample aliquot with 100 % phosphoric acid at 90 °C. The isotope ratios are reported in the delta (δ) notation as the per mil (‰) deviation relative to the Vienna Pee Dee Belemnite limestone (VPDB) standard. The normalization of the measured δ values to the VPDB scale was done with within-run replicate measurements of the laboratory standard Carrara marble ($\delta^{13}C$ = +2.05 ‰, $\delta^{18}O$= − 1.7 ‰), calibrated with international reference materials NBS 18 (carbonatite, $\delta^{13}C$= − 5.04 ‰, $\delta^{18}O$= − 23.00 ‰) and NBS 19 (limestone, $\delta^{13}C$ = +1.95 ‰, $\delta^{18}O$= − 2.19 ‰). The $\delta^{18}O$ values of ankerite samples were corrected for the temperature dependence of the kinetic oxygen isotope fractionation between phosphoric acid-liberated CO_2 and carbonate using the oxygen isotope fractionation equations of Das Sharma et al. (2002) and Rosenbaum & Sheppard (1986). All the $\delta^{18}O$ values were expressed relative to VSMOW (Vienna Standard Mean Ocean Water). Analytical uncertainty (1σ) monitored by replicate analyses of the laboratory standard Carrara marble and NBS 19 was not greater than ± 0.05 ‰ for
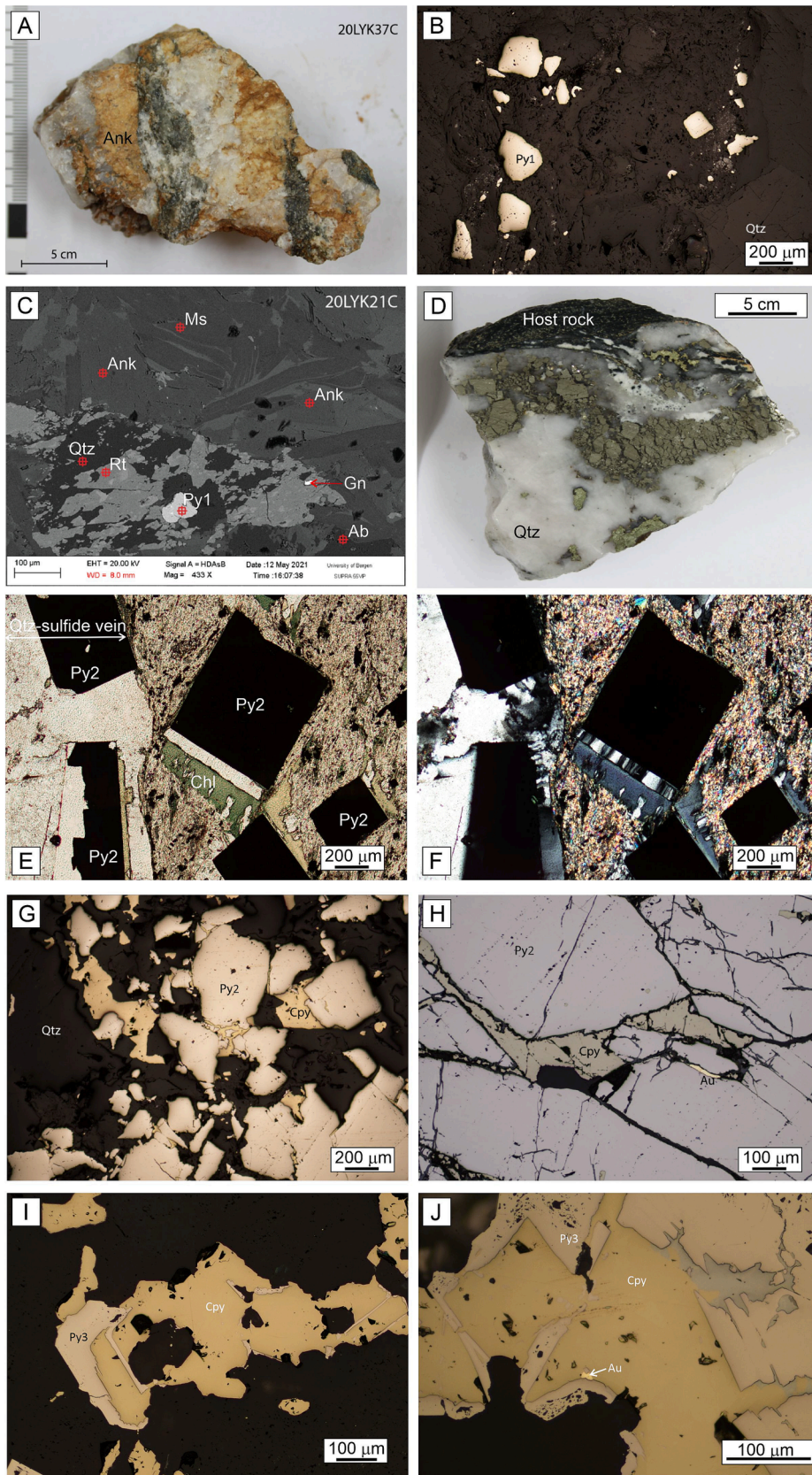
(caption on next page)

Fig. 6. A) A hand specimen of a gold-bearing quartz-carbonate vein; **B)** Reflected light photomicrograph of pyrite (Py1) associated with quartz-carbonate veins hosted by brittle-ductile shear zones, PPL; **C)** Back-scatter electron image of a typical quartz-carbonate vein; **D)** A hand specimen of a quartz-sulfide vein hosted by brittle faults; **E)** Transmitted light photomicrograph of the quartz-sulfide vein in a contact with its host rock shows abundant pyrite (Py2), PPL; **F)** Transmitted light photomicrograph of the quartz-sulfide vein in a contact with its host rock, XPL; **G)** Reflected light photomicrograph of the early generation of pyrite (Py2) and chalcopyrite in the quartz-sulfide vein hosted by brittle faults, PPL; **H)** Reflected light photomicrograph of native gold in the quartz-sulfide vein hosted by brittle faults, PPL.; I) Reflected light photomicrograph of the late generation of pyrite (Py3) overprinting chalcopyrite in a quartz-sulfide vein hosted by brittle faults, PPL; J) Reflected light photomicrograph of a mineral assemblage consisting of chalcopyrite, late generation of pyrite (Py3) and native gold, PPL. Abbreviations: Ab-Albite; Ank-Ankerite; Au-Native gold; Chl-Chlorite; Cpy-Chalcopyrite; Gn-Galena; Ms-Muscovite; Qtz-Quartz; Py-Pyrite; Rt-Rutile.

Table 4
Gold grade obtained from quartz veins at the the Lykling ophiolite-hosted lode Au deposit, SW Norway.

Sample	Type of mineralization	Orientation	Host rock	Au (ppb)
19LYK1A	Brittle-ductile quartz-carbonate	ESE-WNW	Gabbro	17
20LYK15D	Brittle-ductile quartz-carbonate	NNE-SSW	Trondhjemite	4
20LYK21B	Brittle-ductile quartz-carbonate	NNE-SSW	Gabbro	154
20LYK24B	Brittle-ductile quartz-carbonate	ESE-WNW	Trondhjemite	8
20LYK25B	Brittle-ductile quartz-carbonate	NNE-SSW	Trondhjemite	2044
20LYK37C	Brittle-ductile quartz-carbonate	ESE-WNW	Gabbro	240
19LYK2A	Brittle quartz-sulfide	NNE-SSW	Gabbro	107
20LYK4C	Brittle quartz-sulfide	NNE-SSW	Gabbro	275
20LYK13A	Brittle quartz-sulfide	NNE-SSW	Gabbro	4
20LYK18A	Brittle quartz-sulfide	NNE-SSW	Trondhjemite	6
20LYK39A	Brittle quartz-sulfide	ESE-WNW	Gabbro	785
20LYK39C	Brittle quartz-sulfide	ESE-WNW	Gabbro	29,000

δ^{13}C and $\pm$ 0.1 ‰ for δ^{18}O.

Sulfur isotope analyses were carried out at the University of Lausanne, Switzerland, by an elemental analysis and isotope ratio mass spectrometry (EA/IRMS). The EA/IRMS system consisted of a Carlo Erba 1108 elemental analyzer coupled with a continuous helium flow interface to a Thermo Fisher Delta V isotope ratio mass spectrometer (Spangenberg et al., 2022). The samples were combusted in a single oxidation–reduction quartz tube filled with oxidizing (tungsten trioxide) and reducing (elemental copper) agents at 1030 °C. Measured values of sulfur isotopes are given in the δ-notation and relative to the Vienna Cañon Diablo Troilite (VCDT) standard. The laboratory assured reproducibility with replicate analysis with given standards (natural pyrite –6.72 ‰, synthetic mercury sulfide, +15.82 ‰, barium sulfate, +12.73 ‰ δ^{34}S; Spangenberg et al., 2022) to be better than 0.2 ‰.

4. Results

4.1. Country rocks and hydrothermal alteration products

The Lykling Ophiolite gabbro in the study area appears in the form of layered (Fig. 3A) and massive (Fig. 3B) varieties. The layered gabbro is characterized by a rhythmic alternation of melanocratic and leucocratic layers (Fig. 3A). Thickness of the layers varies from a few centimeters up to several meters. Their orientation is strongly affected by folding at a regional scale. The entire Lykling Ophiolite Complex was metamorphosed to greenschist facies during the Caledonian Orogeny. Microscopic investigations revealed that both the massive and layered gabbro in the Lykling area were also hydrothermally altered (Fig. 3C and 3D). Lithogeochemical data obtained for unaltered massive gabbro from the Lykling Ophiolite in the Lykling mineralization area, are listed in Tables 1-3. The samples show a tholeiitic character, exhibiting relatively flat REE patterns with a weak LREE depletion and a very weak negative Eu anomaly (Fig. 4).

Trondhjemite that intruded the Lykling Ophiolite Complex and the Geitung Unit at Bømlo island (Fig. 1) is predominantly composed of quartz and Na-rich plagioclase. Abundant chloritization reflects greenschist facies metamorphism (Fig. 3E). Trondhjemite spatially associated with the gold mineralization records various degrees of saussurization. Minor amounts of disseminated pyrite have been found in hydrothermally altered trondhjemite. Trondhjemite has a calc-alkaline character and shows a gradual enrichment in HREE and a pronounced negative Eu anomaly (Fig. 4).

Two generations of **mafic dykes** crosscut the Lykling Ophiolite gabbro and the associated trondhjemite intrusions. The NNE-SSW
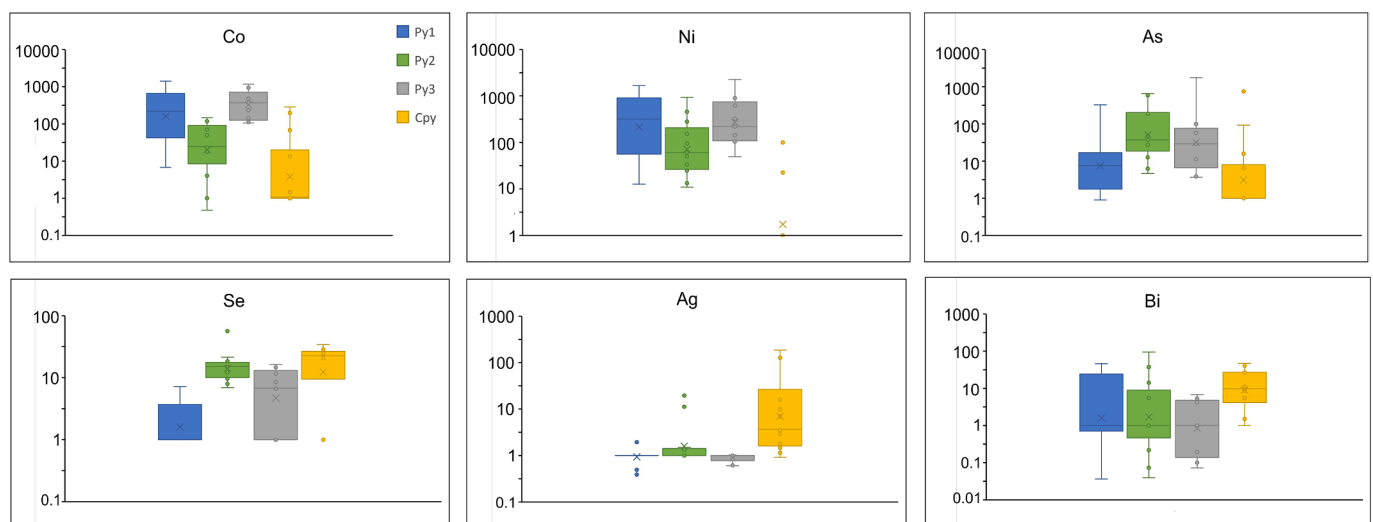

Fig. 7. Trace element composition of the main sulfide phases from the Au-bearing quartz veins at the Lykling ophiolite-hosted lode Au deposit, Norway. Abbreviations: Py1 – Pyrite from the quartz-carbonate veins; Py2 – Early generation of pyrite from the quartz-sulfide veins; Py3 – late generation of pyrite from the quartz-sulfide veins; Cpy – Chalcopyrite from the quartz-sulfide veins.
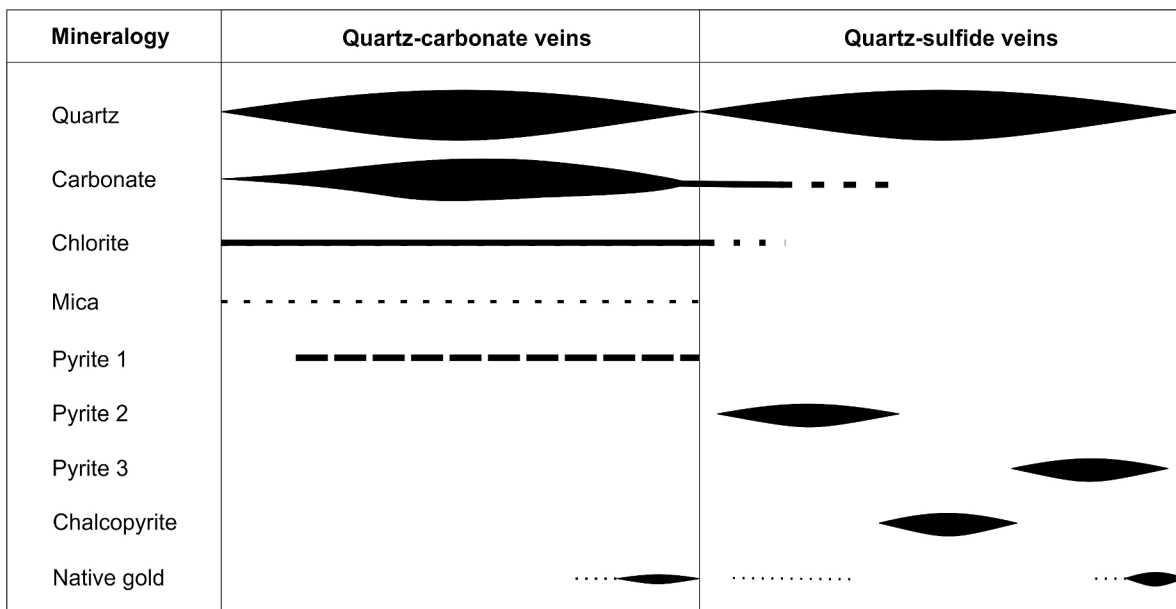
Fig. 8. The paragenetic sequence of the Au-bearing quartz veins at the Lykling ophiolite-hosted lode Au deposit, SW Norway.

Table 5
Carbon and oxygen isotope composition of carbonates from the Au-bearing quartz veins at the Lykling Ophiolite-hosted lode Au deposit, SW Norway.

Sample name	Mineralogy	Type of mineralization	Orientation of the vein	Host rock	$d^{13}C$ (‰; VPDB)	$d^{18}O$ (‰; VPDB)	$d^{18}O$ (‰; VSMOW)
19LYK1A	Ankerite	Brittle-ductile quartz-carbonate	ESE-WNW	Gabbro	−3.7	−18.9	11.4
20LYK3B	Ankerite	Brittle-ductile quartz-carbonate	NNE-SSW	Gabbro	−3.7	−16.9	13.5
20LYK7D	Ankerite	Brittle-ductile quartz-carbonate	NNE-SSW	Gabbro	−4.0	−19.8	10.5
20LYK10C	Ankerite	Brittle-ductile quartz-carbonate	NNE-SSW	Gabbro	−4.1	−20.4	9.9
20LYK15D	Ankerite	Brittle-ductile quartz-carbonate	NNE-SSW	Gabbro	−4.2	−20.4	9.9
20LYK21C	Ankerite	Brittle-ductile quartz-carbonate	NNE-SSW	Gabbro	−4.5	−20.3	10.0
20LYK21B	Ankerite	Brittle-ductile quartz-carbonate	NNE-SSW	Gabbro	−4.4	−20.5	9.8
20LYK24A	Ankerite	Brittle-ductile quartz-carbonate	ESE-WNW	Gabbro	−4.1	−20.1	10.1
20LYK24B	Ankerite	Brittle-ductile quartz-carbonate	ESE-WNW	Gabbro	−4.2	−20.1	10.1
20LYK25B	Ankerite	Brittle-ductile quartz-carbonate	NNE-SSW	Gabbro	−4.0	−20.7	9.6
20LYK37C	Ankerite	Brittle-ductile quartz-carbonate	ESE-WNW	Trondhjemite	−3.8	−19.8	10.5
20LYK6	Ankerite	Brittle quartz-sulfide	NNE-SSW	Gabbro	−3.5	−19.6	10.7
20LYK20J	Ankerite	Brittle quartz-sulfide	NNE-SSW	Trondhjemite	−5.2	−20.8	9.5
20LYK39A	Ankerite	Brittle quartz-sulfide	ESE-WNW	Gabbro	−3.8	−19.7	10.6

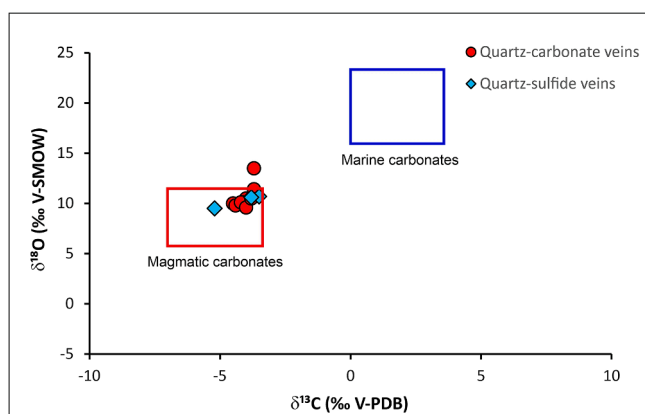**Fig. 9.** $\delta^{18}O$ (VSMOW) vs $\delta^{13}C$ (VPDB) plot illustrating the isotopic composition of carbonates from the quartz-carbonate and quartz-sulfide veins at the Lykling ophiolite-hosted lode Au deposit, SW Norway. The blue box represents isotopic values typical for marine carbonates (Veizer & Hoefs, 1976) and the red box represent the values for magmatic carbonates (Stakes and O'neil, 1982). (For interpretation of the references to colour in this figure legend, the reader is referred to the web version of this article.)

oriented dykes crosscut the ESE-WNW oriented dykes providing a relative age of intrusion (Fig. 2E). The older generation of dykes (ESE-WNW oriented) are coarse grained and highly affected by deformation and faulting (Fig. 2E). The NNE-SSW oriented dykes are fine to medium grained and lighter in colour compared to the ESE-WNW dykes. Both generations of dykes have been subjected to greenschist metamorphism and hydrothermal overprints. The ESE-WNW oriented dykes have a tholeiitic character (Fig. 4). The dykes associated with brittle type structures hosting the Au-bearing quartz-sulfide veins and show a strong depletion in incompatible elements, including LREE. A sample collected in close vicinity to the mineralized brittle-ductile shear zone shows an enrichment in SiO_2, K_2O, Th and La, compared to the dykes associated with the brittle structure hosted mineralization (Fig. 4). In contrast, the younger generation of dykes (NNE-SSW oriented) shows a calc-alkaline character. This generation of the dykes in the Lykling area is characterized by higher SiO_2 and total alkalis and, in general, shows an enrichment in incompatible elements, including LREE, compared to the older generation of mafic dykes (Fig. 4).

The mafic dykes subjected to brittle-ductile shearing and emplacement of mineralized quartz-carbonate veins usually show a hydrothermal overprint recorded by development of hydrothermal alteration halos (Fig. 2A). The XRD analysis suggests quartz, carbonates, chlorite

Table 6

Sulfur isotope composition of sulfides from the Au-bearing quartz veins at the Lykling Ophiolite-hosted lode Au deposit, SW Norway.

Sample name	Mineralogy	Type of mineralization	Orientation of the vein	Host rock	d^{34}C
					(‰; VCDT)
20LYK21B	Py1	Quartz-carbonate vein	NNE-SSW	Trondhjemite	3.1
20LYK27B	Py1	Quartz-carbonate vein	NNE-SSW	Trondhjemite	0.2
20LYK37C	Py1	Quartz-carbonate vein	ESE-WNW	Gabbro	7.2
20LYK14B	Py2	Quartz-sulfide vein	NNE-SSW	Gabbro	6.0
20LYK20B	Py2	Quartz-sulfide vein	NNE-SSW	Trondhjemite	4.8
20LYK39A	Py3	Quartz-sulfide vein	ESE-WNW	Gabbro	7.2
20LYK39C	Py3	Quartz-sulfide vein	ESE-WNW	Gabbro	7.2
20LYK4C	Cpy	Quartz-sulfide vein	NNE-SSW	Gabbro	6.9
20LYK4D	Cpy	Quartz-sulfide vein	NNE-SSW	Gabbro	7.2
20LYK39A	Cpy	Quartz-sulfide vein	ESE-WNW	Gabbro	6.3
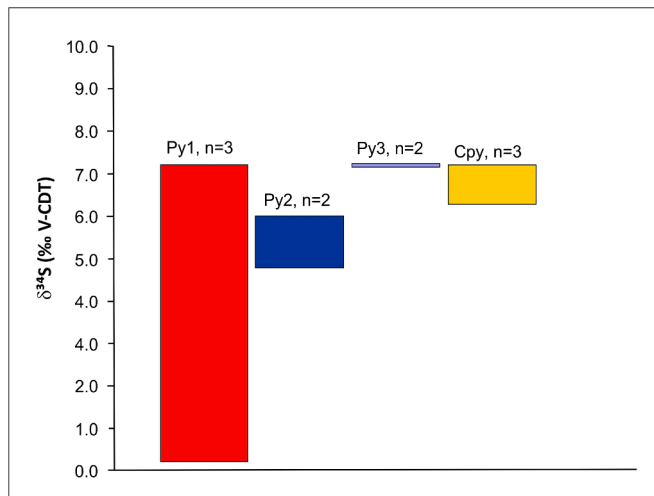
Fig. 10. The δ^{34}S composition of the main sulfide phases from the Au-bearing quartz veins at the Lykling ophiolite-hosted lode Au deposit, SW Norway. Abbreviations: Py1 – Pyrite from the quartz-carbonate veins; Py2 – Early generation of pyrite from the quartz-sulfide veins; Py3 – late generation of pyrite from the quartz-sulfide veins; Cpy – Chalcopyrite from the quartz-sulfide veins.

and epidote as the main constituents of the hydrothermal alteration assemblage (Fig. 5A). The same type of assemblages have been locally found along the contact between the mafic dykes and brittle structure hosted mineralized quartz-sulfide veins (Fig. 5B).

4.2. Petrography of the ore mineralization and the Au grade

The quartz-carbonate veins hosted by brittle-ductile shear zones consist predominantly of milky quartz pods associated with abundant carbonate of an ankeritic composition and variable amounts of hydrous silicates, mostly chlorite (Fig. 6A). Reflected light microscopy supported by SEM/EDS analysis also revealed the presence of disseminated pyrite (Fig. 6B) and minor amounts of rutile, albite, muscovite and rare galena grains (Fig. 6C). Pyrite (Pyrite 1, hereafter Py1) occurs in the form of euhedral to subhedral grains ranging in size from <10 μm up to 1 cm (Fig. 6B and 6C). Free gold has not been observed. The ore grade analyses revealed that the concentration of Au in this type of mineralization reaches up to 2 g/t (Table 4).

The quartz-sulfide veins hosted by brittle faults are composed of quartz and variable amounts of sulfides, predominantly pyrite and chalcopyrite (Fig. 6D-G). The vein-host rock contacts are sharp and hydrothermal alteration halos are mostly absent. Anyhow, microscopical examinations reveal that the host rocks were subjected to a limited infiltration of the hydrothermal fluids, resulting in precipitation of hydrothermal chlorite and pyrite (Fig. 6E and 6F). The quartz grains along the vein-host rock contacts show a perpendicular growth (Fig. 6E) but

the preferential orientation seems to be lost towards the central portion of the quartz-sulfide veins. Reflected light microscopy and SEM/EDS mapping show a presence of at least two generation of pyrite, one that predates chalcopyrite (Pyrite 2, hereafter Py2) and one that postdates chalcopyrite deposition (Pyrite 3, hereafter Py3). The sulfide mineralization is accompanied by native gold (Fig. 6H and 6J). The ore grade analyses yielded highly variable Au concentrations ranging between 4 mg/t up to 29 g/t (Table 4).

4.3. Trace element composition of sulfide phases

Pyrite from **the quartz-carbonate veins hosted by brittle-ductile shear zones** (Py1) shows an enrichment in Ni (12.7–1677 ppm, the mean value at 480 ppm) and Co (6.8–1414 ppm, the mean value at 393 ppm; Fig. 7). The Au content was below the detection limit in all analysed points (Appendix 2). The trace element maps revealed a refractory nature of Co, Ni, As and Se in pyrite (Appendix 3). Gold occurs in forms of micron-sized inclusions within individual pyrite grains and shows the spatial correlation with Ag, Te and Cu. Gold also has been identified along cracks and grain boundaries of pyrite (Appendix 3). Bismuth, Mo and Pb are enriched along pyrite grains (Appendix 3) indicating their deposition late in the paragenesis (Fig. 8).

The older generation of pyrite from **the quartz-sulfide veins hosted by brittle faults** (Py2) is characterized by an enrichment in Se (up to 57 ppm) and Ag (up to 20 ppm), while the late pyrite (Py3) shows an enrichment in Co, Ni and As (Appendix 2, Fig. 7). In comparison to both generations of pyrite, chalcopyrite is enriched in Zn, Ag and Pb, but depleted in Co, Ni and As (Appendix 2, Fig. 7). Trace element mapping supports the refractory character of Co, Ni and As in the older generation of pyrite. Native gold occurs in the form of micron-sized inclusions within individual grains of Py2, spatially correlating with Ag and Se, and in form of nuggets that overprint the younger Py3 (Appendix 3).

4.4. Stable isotope geochemistry

The stable isotope compositions of carbonates (δ^{13}C vs. δ^{18}O) sub-sampled from the mineralized quartz-carbonate and quartz-sulfide veins are listed in Table 5. Ankerite from the quartz-carbonate veins yielded δ^{13}C and δ^{18}O values in the range between −4.5 and −3.7 ‰ VPDB and + 9.6 and + 13.5 ‰ VSMOW, respectively. Ankerite from the quartz-sulfide veins is characterized by δ^{13}C values between −5.2 and −3.5 ‰ VPDB and the δ^{18}O values between + 9.5 and + 10.7 ‰ VSMOW. The obtained results reflect a magmatic source of CO$_2$ without a significant difference in the isotopic composition of carbonates from the two main types of Au-bearing veins at the Lykling Ophiolite-hosted lode Au deposit (Fig. 9).

The δ^{34}S values obtained for the main sulfide phases from the Lykling Ophiolite-hosted lode Au deposit are listed in Table 6. Pyrite from the quartz-carbonate veins (Py1) shows values between 0.2 and 7.2 ‰ VCDT, while sulfides (Py2, Py3 and Chalcopyrite) from the quartz-sulfide veins yielded values between 4.8 and 7.2 ‰ VCDT (Fig. 10).
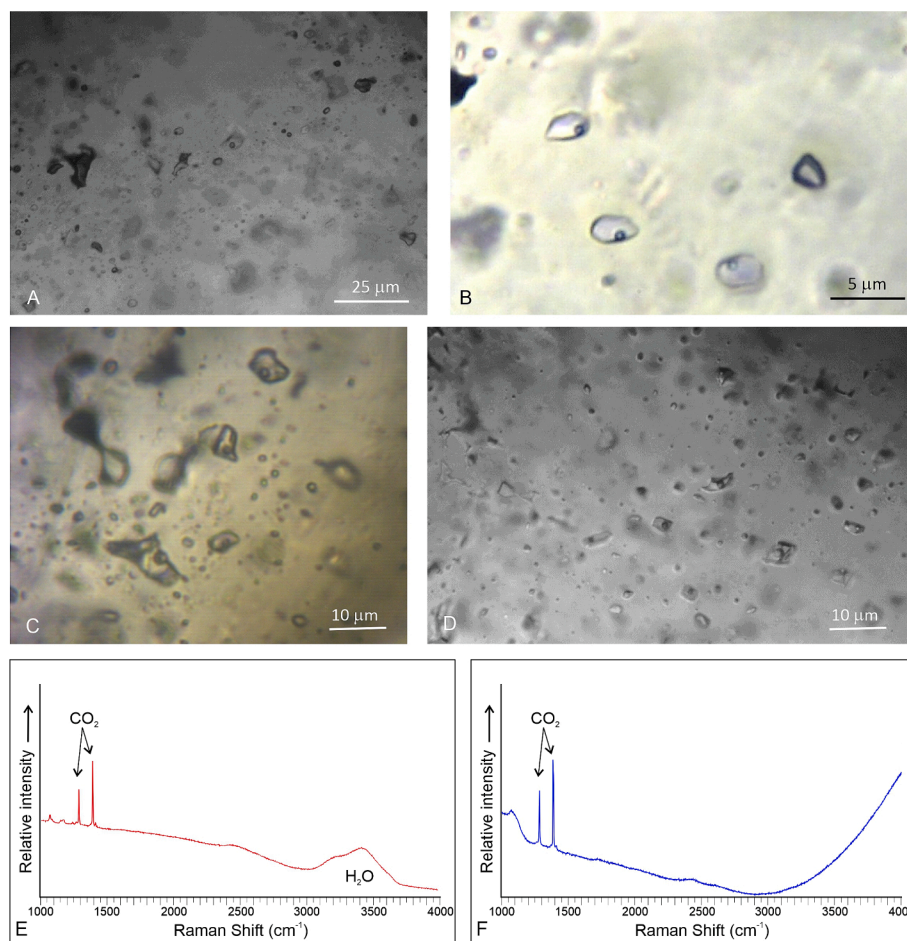
Fig. 11. A) Type 1A fluid inclusion assemblages in the quartz-carbonate veins; **B)** Type 2 fluid inclusion assemblages in the quartz-carbonate veins; **C)** Type 3 fluid inclusion assemblages in the quartz-sulfide veins; **D)** Type 3 fluid inclusion assemblages in the quartz-sulfide veins; E) A representative Raman spectrum obtained from the vapour phase of a Type 1A fluid inclusion; F) A representative Raman spectrum obtained from a vapour-rich fluid inclusion hosted by a Type 2 fluid inclusion assemblages.

4.5. Fluid inclusion study

In total, 153 fluid inclusions from 33 fluid inclusion assemblages were measured in quartz separated from the quartz-carbonate and quartz-sulfide veins. The complete dataset is listed in Appendix 4.

In addition to quartz, carbonate grains from the quartz-carbonate veins were prepared for the fluid inclusion study, but they contained only decrepitated fluid inclusion assemblages. In contrast, quartz grains from same hand specimens, in addition to decrepitated fluid inclusion assemblages, often have preserved two types of fluid inclusion assemblages: 1) Type 1 – Fluid inclusion assemblages that at the room temperature consist of two phases (liquid + vapour) and show an uniform degree of fill (F) around 0.8 (Fig. 11A) and 2) Type 2 – Fluid inclusion assemblages that at the room temperature record the coexistence of liquid-rich and vapour-rich inclusions reflecting an entrapment under boiling conditions (Fig. 11B). In general, fluid inclusion assemblages that do not show decrepitation phenomena contain only small fluid inclusions, usually with their sizes below 5 μm (Fig. 11A and 11B).

In both types of the fluid inclusion assemblages the first melting was observed around −52 °C suggesting a $CaCl_2$-NaCl-H_2O system (Vanko et al, 1988). Type 1 FIAs shows the last ice melting temperatures in the range between −1.9 and −4.3 °C corresponding to the bulk salinity of 3.2 to 6.9 wt% NaCl eq. The total homogenization (Th) into the liquid phase is recorded in a broad interval between 120 and 185 °C. The salinity vs. homogenization temperature (Th) diagram (Fig. 12) revealed that the fluid inclusions of this type can be subdivided into a higher-

temperature sub-type (Type 1A) with Th between 165 and 185 °C and the lower-temperature sub-type (Type 1B) with Th between 120 and 135 °C. The higher-temperature sub-type is characterized by a slightly lower salinities (3.2–6.5 wt% NaCl eq.) comparing to the low-temperature sub-type (5.0–6.9 wt% NaCl eq.). Although clathrates have not been observed during microthermometric measurements, the Raman spectroscopy revealed traces of CO_2 in fluid inclusions of the higher-temperature sub-type (Fig. 11E; Forsberg, 2021) suggesting the maximum CO_2 concentration of 1.5 mol% (Diamond, 2001; Bauer et al., 2018).

Type 2 FIAs are composed of coexisting liquid- and vapour rich-inclusions. This type of assemblages is relatively common in the quartz-carbonate veins but only a few FIAs were suitable for the microthermometric measurements of the total homogenization temperature in the vapour-rich inclusions (Appendix 4). The liquid-rich inclusions show the first melting around −52 °C and the last ice melting between −3.0 and −3.5 °C indicating the salinity range from 5.0 to 5.7 wt% NaCl eq. Their homogenization temperature spans between 165 and 170 °C and overlaps with those observed in the coexisting vapour-rich inclusions (Appendix 4). The Raman spectroscopy has not recorded a presence of CO_2 in the liquid-rich inclusions, but the associated vapour-rich inclusions contain detectable amounts of CO_2, suggesting that this type of FIAs may record a phase separation of NaCl-$CaCl_2$-H_2O ±CO_2 fluids represented by Type 1A FIAs (Fig. 11F).

Quartz grains separated from the quartz-sulfide veins mostly contains two-phase (L+V) fluid inclusions with the degree of fill between
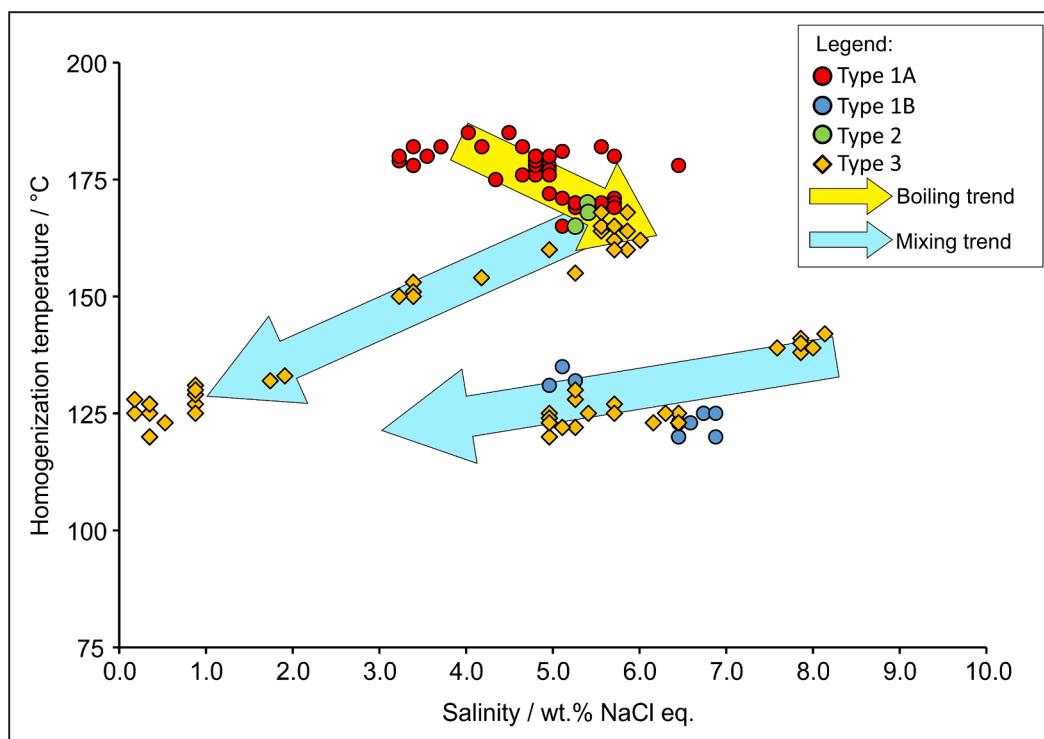
Fig. 12. Correlation of homogenization temperature and salinity for fluid inclusions hosted by the quartz-carbonate and quartz-sulfide veins at the Lykling ophiolite-hosted lode Au deposit, SW Norway.

0.7 and 0.85 (Fig. 11C). Decrepitated fluid inclusion assemblages have also been recorded (Fig. 11D) and, similar to the fluid inclusion assemblages hosted by quartz in the quartz-carbonate veins, only fluid inclusion with the size <5 μm are preserved. The microthermometric measurements revealed that the two-phase inclusions (Type 3) show a broad range of salinities (0.2–12.2 wt% NaCl eq.) and homogenization temperatures (120–189 °C). The eutectic temperatures were recorded only for several FIAs and they indicate presence of $NaCl-CaCl_2-H_2O$ and $NaCl-H_2O$ fluids (Appendix 3). Raman spectroscopy analysis has not detected any CO_2 (Forsberg, 2021). The salinity vs. Th diagram (Fig. 12) reflects a mixing of moderate-salinity and higher-temperature fluids with diluted and colder fluids.

4.6. Chlorite geothermometry

The chemical composition of chlorite was determined with an aim to estimate the formation temperature of the quartz-carbonate veins. The analysis was performed on chlorite grains that represent a part of the hydrothermal alteration assemblage associated with the deposition of the gold-bearing veins. All analysed chlorite show the clinochlore composition (Table 7). The geothermometer proposed by Cathelineau (1998) yielded the crystallization temperature between 309 and 329 °C (Table 7).

5. Discussion

The Lykling lode Au mineralization is hosted by the Early Ordovician Lykling Ophiolite Complex and associated trondhjemite. The mineralization is spatially associated with two generations of mafic dykes. The older generation of the dykes shows an ESE-WNW orientation and has a tholeiitic character. The geochemical signature suggests that this generation of dykes is genetically linked to the Lykling Ophiolite Complex (Tables 1–3). The younger generation of the dykes has a NNE-SSW orientation and it is characterized by a calc-alkaline signature (Fig. 6). The geochemical characteristics (Tables 1–3) link this generation of the

dykes with emplacement of the 473 ± 2 Ma Siggjo Complex (e.g., Furnes et al., 1986; Pedersen & Dunning, 1997). The cross-cutting relationships of the mineralized quartz veins and the mafic dykes (Fig. 4) suggest that emplacement of the dykes did not have any active role in the formation of the Lykling ophiolite-hosted lode Au deposit. The lithological contacts of the dykes with their immediate host rocks (i.e., gabbro and trondhjemite) rather could have served as channels for the focused ore-forming fluid flow emplacing the hydrothetmal veins along these contacts. The observed cross-cutting relationships also constrain the age of the Lykling lode Au mineralization to a maximum of 473 ± 2 Ma (Pedersen & Dunning, 1997).

The evolution of the hydrothermal system in the Lykling area is documented by two generations of hydrothermal veins: 1) older quartz-carbonate veins hosted by moderately dipping brittle-ductile shear zones and 2) younger quartz-sulfide veins that fill steeply dipping brittle faults (Fig. 4).

5.1. The quartz-carbonate gold-bearing veins

The quartz-carbonate veins hosted by the shear zones in the Lykling area record multiple episodes of ductile deformations and brecciations typical for brittle-ductile environments (e.g., Groves et al., 1998). A prevalence of quartz and Fe-rich carbonates, a low sulfide mineral content, hydrothermal alteration assemblages with abundant carbonates, chlorites and micas (Fig. 10) as well as a spatial association with shear zones and metamorphosed host lithologies have been identified as common characteristics of orogenic gold deposits elsewhere (e.g., Zoheir et al., 2019b; Groves et al., 2020; Tavares Nassif et al., 2022).

The isotopic signature of carbonates reflects a magmatic source of CO_2 (Table 5, Fig. 9). The $\delta^{34}S$ composition of pyrite in the range between 0.2 and 7.2 ‰ (Table 6) does not unequivocally distinguish the source of sulfur but it overlaps with values reported for basalt-hosted sulfide deposits elsewhere as well as with values common for sulfides precipitated from exsolved magmatic fluids (e.g., Kerrich, 1986; Hoefs, 2009; Strmić Palinkaš et al., 2024). In contrast, orogenic gold deposits

Table 7
Chemical composition of chlorite from the quartz-carbonate veins at the Lykling ophiolite-hosted lode Au deposit, SW Norway.

	20LYK-3B (Quartz-carbonate vein)								20LYK10C (Quartz-carbonate vein)				20LYK21B (Quartz-carbonate vein)					
	Spot#1	Spot#2	Spot#3	Spot#4	Spot#5	Spot#6	Spot#7	Spot#8	Spot #1	Spot #2	Spot #3	Spot #4	Spot #1	Spot #2	Spot #3	Spot #4	Spot #5	Spot #6
SiO2	27.30	26.95	27.07	27.33	26.99	27.05	27.01	27.17	26.22	26.61	26.31	26.25	27.11	27.05	27.15	27.22	27.25	27.10
TiO2	<d.l.	<d.l.	<d.l.	<d.l.	<d.l.	<d.l.	<d.l.	<d.l.	<d.l.	<d.l.	<d.l.	<d.l.	<d.l.	<d.l.	<d.l.	<d.l.	<d.l.	<d.l.
Al2O3	19.21	18.79	18.67	18.37	18.57	18.22	18.99	19.11	17.15	17.22	17.24	17.65	18.52	18.55	18.99	18.97	18.44	18.69
Cr2O3	<d.l.	<d.l.	<d.l.	<d.l.	<d.l.	<d.l.	<d.l.	<d.l.	<d.l.	<d.l.	<d.l.	<d.l.	<d.l.	<d.l.	<d.l.	<d.l.	<d.l.	<d.l.
Fe2O3	0.16	<d.l.	<d.l.	<d.l.	<d.l.	<d.l.	<d.l.	<d.l.	<d.l.	<d.l.	<d.l.	<d.l.	<d.l.	<d.l.	<d.l.	<d.l.	<d.l.	<d.l.
FeO	26.36	27.00	26.27	26.21	26.55	26.15	26.26	26.19	30.46	31.13	31.65	31.25	27.37	27.45	27.42	27.65	27.55	27.07
MnO	<d.l.	<d.l.	<d.l.	<d.l.	<d.l.	<d.l.	<d.l.	<d.l.	<d.l.	<d.l.	<d.l.	<d.l.	<d.l.	<d.l.	<d.l.	<d.l.	<d.l.	<d.l.
MgO	16.11	15.93	16.81	16.88	16.56	17.08	16.47	16.45	15.07	14.43	14.05	14.15	15.77	15.65	15.75	15.76	16.02	16.44
F	<d.l.	<d.l.	<d.l.	<d.l.	<d.l.	<d.l.	<d.l.	<d.l.	<d.l.	<d.l.	<d.l.	<d.l.	<d.l.	<d.l.	<d.l.	<d.l.	<d.l.	<d.l.
Cl	<d.l.	<d.l.	<d.l.	<d.l.	<d.l.	<d.l.	<d.l.	<d.l.	<d.l.	<d.l.	<d.l.	<d.l.	<d.l.	<d.l.	<d.l.	<d.l.	<d.l.	<d.l.
H2O*	11.54	11.43	11.49	11.50	11.45	11.45	11.49	11.53	11.20	11.24	11.18	11.22	11.42	11.41	11.50	11.53	11.48	11.51
Total	100.69	100.10	100.31	100.29	100.12	99.95	100.22	100.45	100.10	100.63	100.43	100.52	100.19	100.11	100.81	101.13	100.74	100.81
Temp*/°C	313	316	318	309	318	316	319	316	329	317	323	327	310	311	315	315	311	319

Reformatted oxide percentages based on 28 oxygens (with Fe^{2+}/Fe^{3+} and OH calculated assuming full site occupancy)

* Temperature calculated from the chlorite composition based on the geothermometry by Cathelineau (1988).

usually show a slight shift towards negative $\delta^{34}S$ values, predominantly controlled by fluid/sediment interactions (e.g. Ridley & Diamond, 2000; Hart et al., 2002; Bark et al., 2021). The high carbonate/sulfide ratio in this type of veins indicates a high f_{CO2}/f_{S2} ratio presumably controlled by the difference in solubility of CO_2 and S in silicate melts. The shift in deposition of magmatic carbonates prior to sulfides has been recognized in magmatic-hydrothermal deposits during episodes of limited magma degassing, for example, under conditions of a high confining pressure (Burgisser et al., 2015; Strmić Palinkaš et al., 2018). The magmatic signatures of volatiles together with the high carbonate/sulfide ratio point to a link between the quartz-carbonate veins and an early stage of magmatic activity in the area. The field observations and the regional geological setting of the Lykling mineralization suggest that this generation of quartz veins may be concomitant with the early stages of emplacement of the Sunnhordland Batholith (Andersen et al., 1991).

Fluid inclusions reveal that the quartz-carbonate in veins were deposited from moderately saline NaCl-CaCl2-H2O±CO2 fluids (Appendix 4) under conditions of variable pressure (Fig. 12). The decrepitated FIAs observed in orogenic gold deposits elsewhere have been considered as indicators of post-entrapment modification of fluid inclusions originally formed under higher supra-lithostatic pressures but evolved to near-hydrostatic conditions due to either cooling of the metamorphic belt and the associated downward migration of the brittle-ductile transition boundary or due to regional uplift and exhumation of a terrain (Sibson & Scott, 1998; Vry et al., 2010; White et al., 2015; Tavares Nassif et al., 2022). Carbonate minerals from the Lykling quartz-carbonate veins have experienced complete decrepitation of their primary FIAs, while quartz still preserves some FIAs probably reflecting competency contrasts between the two minerals.

Isochores modeled for Type 1A FIAs (NaCl-CaCl2-H2O±CO2 fluids; Th = 165 and 185 °C, 3.2——6.5 wt% NaCl eq.) accompanied with the chlorite geothermometry data (~310–330 °C) suggest that these FIAs were entrapped at pressures between 2.7 and 3.5 kbar suggesting formation at depths between 10 and 13 km assuming an entirely lithostatic regime (Fig. 13). The coexistence of chlorite, minor amounts of mica and ankerite together with the absence of calcite indicate that the pH of mineralizing fluids was mildly acidic. Thermodynamic modelling reveals that at the given physicochemical conditions, Au was likely transported in the form of Au-chloride complexes (Stage 2, Fig. 14) supported by the lack of refractory Au in pyrite from the Lykling quartz-carbonate veins (Py1; Fig. 8). The Type 1B FIAs likely reflect cooling of the system, presumably still under lithostatic conditions (Arrow 1, Fig. 13) but P-T conditions of their entrapment have not been determined.

The presence of Type 2 FIAs (coexisting liquid-rich aqueous fluid inclusions and vapour-rich CO2-bearing fluid inclusions; Appendix 4) points to a significant decrease in pressure that resulted in phase separation at approximate conditions of 160 bar and 165 to 175 °C (Arrow 2, Fig. 13). The decrease in pressure can be attributed to uplift of the ophiolite complex and mineralizing system across the crustal brittle-ductile transition zone, evolving towards hydrostatic pressure controls on the system (e.g., Zoheir et al., 2018; Tavares Nassif et al., 2022). The decrease in temperature may reflect an adiabatic phase separation. Under these P-T conditions stability of Au-bisulfide complex is favoured over Au-chloride complexes (Stage 2, Fig. 14) making the hydrothermal mobility of gold sensitive to f_{S2}, temperature, and pH (e.g., Seward et al., 2014):

$$Au(HS)_2^- + 2H^+ \leftrightarrow Au^0 + H_2S \ (g)$$
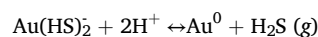
The presence of native gold in cracks and along surfaces of individual pyrite grains in the quartz-carbonate veins (Appendix 3) is indicative for the deposition of Au promoted by the decompression of the system and subsequent loss of H_2S. Textural features of the quartz-carbonate veins record multiple episodes of plastic deformation followed by brecciation and fluid discharge, indicating that the system was exposed to pressure
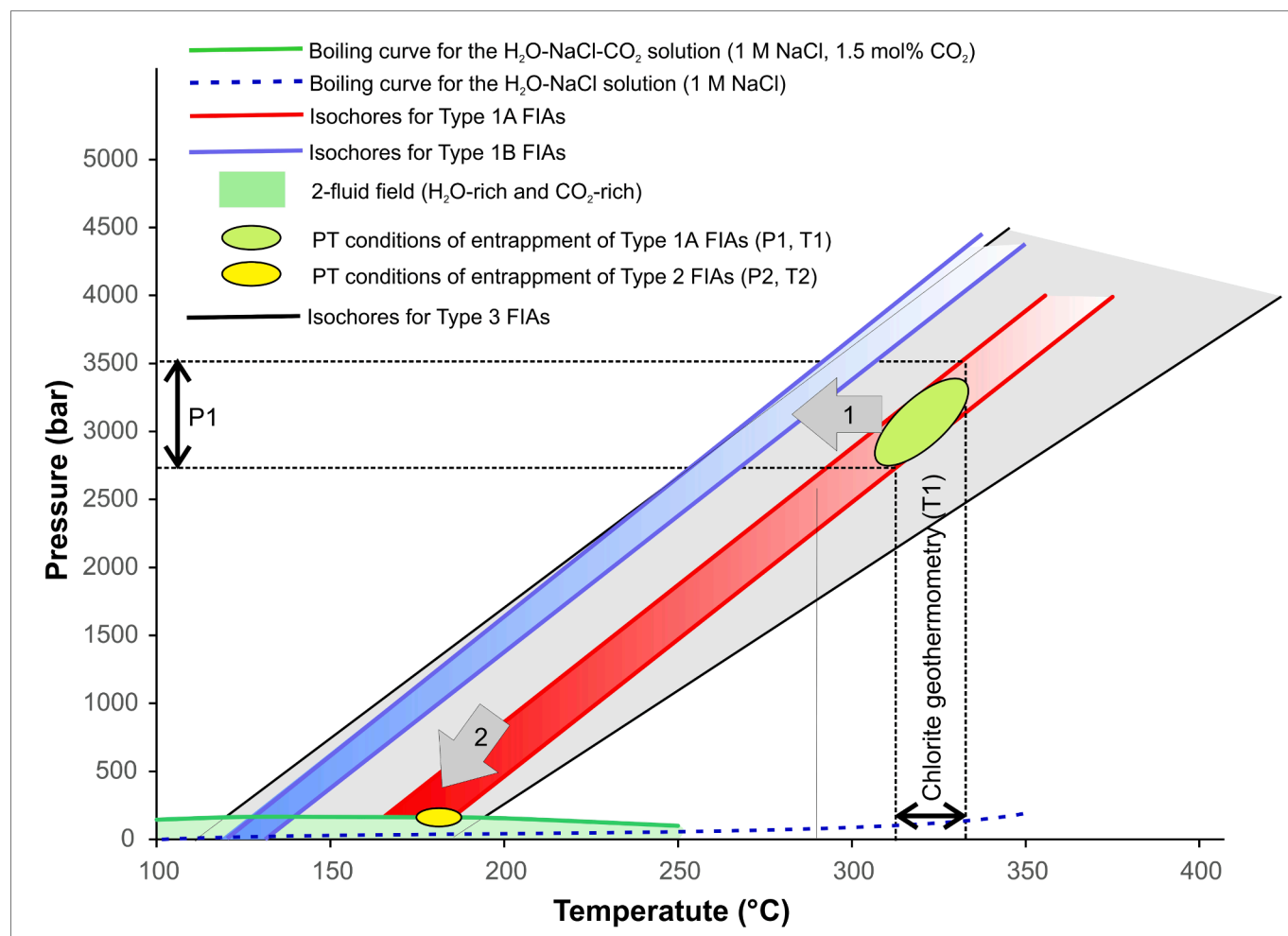
Fig. 13. The P-T diagram showing the endmember isochores constructed for the quartz-carbonate and quartz-sulfide veins at the Lykling ophiolite-hosted lode Au deposit, SW Norway. The exact entrapment conditions for the earliest generation of the fluid inclusions in the quartz-carbonate (Type 1A) have been estimated from intersections of the representative isochores and obtained chlorite geothermometry. The boiling curve for the H2O-NaCl-CO2 system is calculated based on the model proposed by Dubacq et al. (2013).

variations spanning lithostatic to hydrostatic conditions over a protracted period of time.

5.2. The quartz-sulfide gold-bearing veins

The quartz-sulfide veins are hosted by brittle faults in the Lykling area (Fig. 2). This generation of gold-bearing veins crosscut the quartz-carbonate veins defining their relative age during the formation of the Lykling ophiolite-hosted lode Au deposit. Their steeply dipping orientation accompanied by open-space filling textures indicate the formation under extensional conditions.

In contrast to the earlier formed quartz-carbonate veins, the quartz-sulfide veins are characterized by a high sulfide/carbonate ratio. The isotopic signature of carbonates overlaps with the signature of carbonates from the quartz-carbonate veins (Table 5, Fig. 10) reflecting a magmatic source of CO2. The isotopic composition of pyrite and chalcopyrite shows a slight shift toward more positive $\delta^{34}S$ values (Table 6).

The fluid inclusion assemblages from quartz in the quartz-sufide veins reflect a mixing of moderate-salinity and higher-temperature fluids with diluted and colder fluids as the main mechanism for deposition of this type of the veins. Two parallel mixing trends shown in Fig. 12 may point to the multiple fluxes of the hot and saline fluids.

The veins carry two generations of pyrite and a single generation of chalcopyrite (Fig. 8). The older generation of pyrite (Py2) is enriched in

As, Se, and Ag and depleted in Co, Ni and Bi compering to the younger generation of pyrite from the quartz-sulfide veins (Py3; Fig. 8). Also, the older generation of pyrite may contain up to 1.1 ppm of Au and represents the only type of pyrite in the Lykling ophiolite-hosted lode Au deposit with detectable amounts of Au in its crystal lattice (Appendix 2). The break between deposition of Py2 and Py3 is marked by precipitation of variable amounts of chalcopyrite (Fig. 8) suggesting a fluctuation in composition and/or temperature of the mineralizing fluids. Gold is mostly deposited in its native form relatively late in the paragenetic sequence (Fig. 8).

5.3. The ore-forming model for the Lykling ophiolite-hosted lode Au deposit

Numerous studies have documented orogenic gold formation under conditions of variable pressure (e.g., Sibson et al., 1988; Sibson, 2004; Zoheir et al., 2019c), but mechanisms that take into consideration temporal changes in pressure at the scale of a single deposit has been proposed only recently for the Garrcon orogenic Au deposit in the Abitibi greenstone belt, Canada (Tavares Nassif et al., 2022).

Similar to the Garrcon deposit, the Lykling ophiolite-hosted lode Au deposit records temporal changes in the pressure regime and their role in the deposition of Au in this type of mineral deposits. Paragenetically older quartz-carbonate veins were deposited from a focused fluid flow
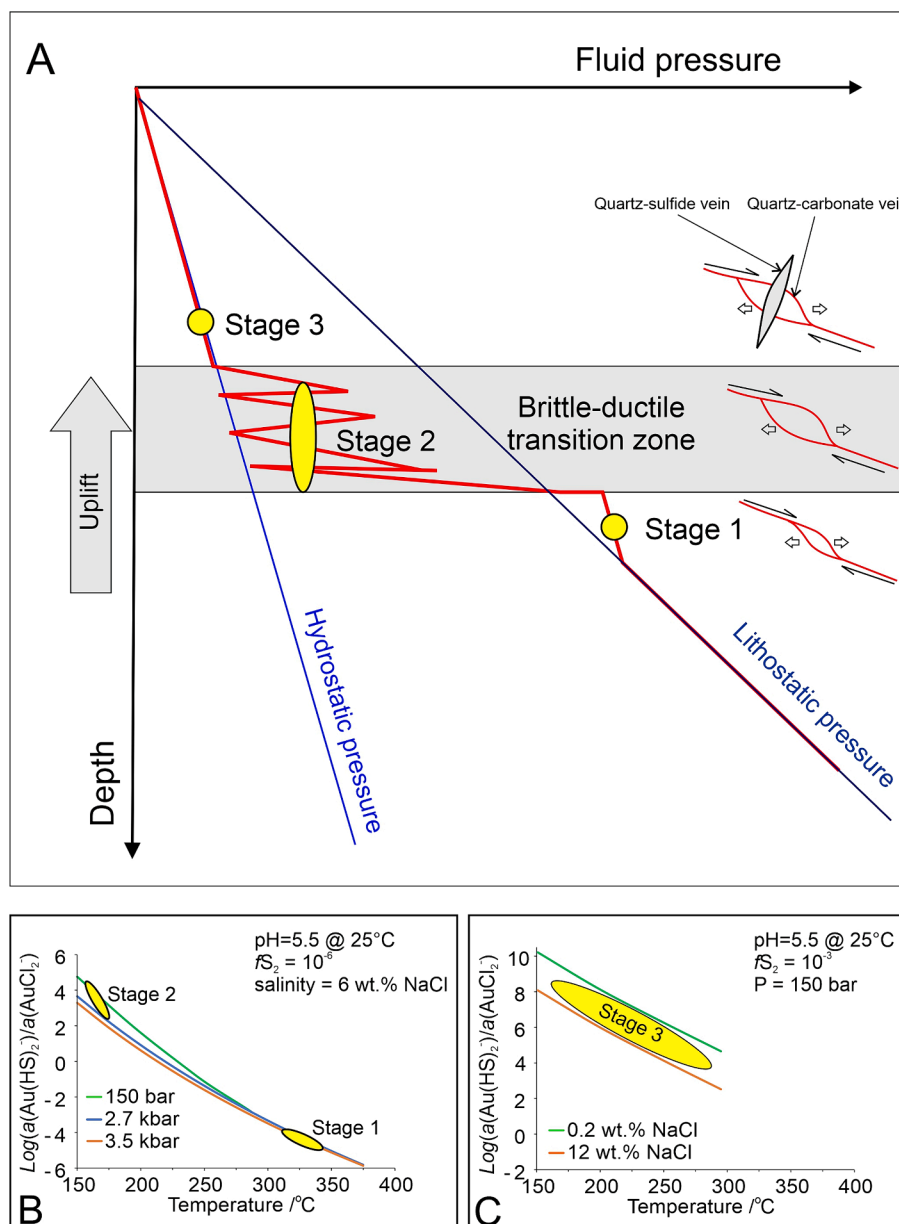
Fig. 14. A) The depth-fluid pressure model illustrating the development of the Lykling ophiolite-hosted lode Au deposit, SW Norway. Modified after Sibson (2020) and Tavares Nassif (2022); B) The Au-complexes stability during formation of the quartz-carbonate veins at the Lykling ophiolite-hosted lode Au deposit, SW Norway as a function of temperature, pressure, sulfur fugacity, pH value of the fluid and the fluid salinity); C) The Au-complexes stability during formation of the quartz-sulfide veins at the Lykling ophiolite-hosted lode Au deposit, SW Norway as a function of temperature, pressure, sulfur fugacity, pH value of the fluid and the fluid salinity. The thermodynamical modelling was preformed using the SUPCRT model and the associated databases (Johnson et al. 1992).

along moderately dipping shear zones. The earliest mineralizing fluids were moderately saline $NaCl-CaCl_2-H_2O\pm CO_2$ solutions with temperatures between 310 and 330 °C and the fluid pressure between 2.7 and 3.5 kbar. During this stage Au was mobile in the form of Au-chloride complexes (Stage 1, Fig. 14).

The multiple episodes of ductile deformations interrupted by periods of fragmentations and brecciation suggest that the system was subjected to the brittle-ductile transition processes. The transition from the ductile to brittle regime resulted with the decompression of the system and the fluid separation to the high-dense $NaCl-CaCl_2-H_2O$ and low-dense H_2O $\pm CO_2$ phases. The decreased temperature and pressure resulted with stabilization of the Au-bisulfide complex making the hydrothermal mobility of Au sensitive to pressure changes (Stage 2, Fig. 14).

Paragenetically younger quartz-sulfide veins indicate that the latest stage of the Au mineralization in the Lykling deposit occurred under

brittle conditions (Stage 3, Fig. 14) presumably due to the progressive uplift of the Lykling area (e.g., Tavares Nassif et al., 2022). The fluid inclusion study revealed a mixing of higher-temperature and moderate-salinity fluids with colder and diluted fluids as the principal trigger for deposition of sulfides and gold in this generation of veins in the Lykling area.

Similar to numerous orogenic gold deposits elsewhere, the Lykling ophiolite-hosted lode Au deposit is hosted by regionally metamorphosed fertile oceanic crust (Goldfarb et al., 1993; Goldfarb et al., 2005; Phillips & Powell, 2010; Goldfarb & Pitcairn, 2023). The mineralization is spatially associated with two generations of mafic dykes that crosscut the Early Ordovician Lykling Ophiolite Complex and associated trondhjemite. Emplacement of the dykes did not have an active role in deposition of the gold-bearing veins but their contact with the immediate host rocks (i.e., gabbro and trondhjemite) rather served as

lithologically weak zones that channelled the focused ore-forming fluid flow.

In contrast to the great majority of the known orogenic gold deposits (e.g., Goldfarb & Pitcairn, 2023), the Lykling ophiolite-hosted lode Au deposit records a magmatic origin of CO_2. In addition, the $\delta^{34}S$ signature of sulfide phases plausibly reflects an input of magmatic sulfur. Therefore, taking into the consideration the field relationships and the regional geology setting of the Lykling deposit, we argue that its formation may be concomitant with emplacement of the Sunnhordland Batholith (Fig. 1B) during the post-collisional thinning of the crust and the associated uplift of the Ophiolite Complex.

6. Conclusions

The Lykling ophiolite-hosted lode Au mineralization is located within the Upper Allochthone of the Scandinavian Caledonides. The mineralization is deposited in the form of: 1) Paragenetically older quartz-carbonate veins that are hosted by moderately dipping shear zones of a mixed brittle-ductile character; and 2) Paragenetically younger quartz-sulfide veins that fill steeply dipping brittle faults.

The quartz-carbonate veins are embedded within a hydrothermal alteration halo that consists of carbonates, chlorites, epidote, micas and minor amounts of pyrite. The mineralizing fluids had a slightly acidic character and a high fCO_2/fS_2 ratio. The paragenetically earliest quartz was deposited from moderately saline $NaCl-CaCl_2-H_2O\pm CO_2$ fluids at temperatures between ~ 310–330 °C and pressures in the range from 2.7 to 3.5 kbars. Under the given physicochemical conditions Au was mobile in the form of chloride complexes. This generation of the auriferous quartz veins also documents multiple episodes of ductile deformations interrupted by periods of fragmentations and brecciation suggesting that the system was subjected to brittle-ductile transition processes. The transition from the ductile to the brittle regime is also supported by the presence of FIAs that record phase separation of high-dense $NaCl-CaCl_2-H_2O$ and low-dense $H_2O\pm CO_2$ fluids. The decreased temperature and pressure resulted with stabilization of the Au-bisulfide complex making the hydrothermal mobility of Au sensitive to pressure changes. Consequently, gold occurs in forms of micron-sized inclusions within individual pyrite grains showing the spatial correlation with Ag, Te and Cu, and along cracks and surfaces of individual pyrite grains.

The quartz-sulfide veins record open-space deposition under brittle conditions. The mineral assemblage points to a significant decrease in the fCO_2/fS_2 ratio. The fluid inclusion study revealed a mixing of higher-temperature and moderate-salinity fluids with colder and dilute fluids as the principal trigger for deposition of sulfides and gold in this generation of veins in the Lykling area.

The Lykling ophiolite-hosted lode Au deposit shows numerous similarities with orogenic gold deposits elsewhere, including the structural control during the mineralizing events, deposition from moderately to low saline CO_2-bearing aqueous solutions, the deposition from a focused fluid flow along *trans*-crustal fault zones of mixed brittle-ductile character and a spatial association with regionally metamorphosed terranes.

Anyhow, in contrast to the great majority of the known orogenic gold deposits, the Lykling ophiolite-hosted lode Au deposit records a magmatic origin of volatiles. Therefore, taking into the consideration the field relationships and the regional setting of the Lykling deposit, we argue that its formation might have occurred simultaneously with emplacement of the Sunnhordland Batholith during the post-collisional thinning of the crust and the associated uplift.

Declaration of competing interest

The authors declare that they have no known competing financial interests or personal relationships that could have appeared to influence the work reported in this paper.

Data availability

Data will be made available on request.

Acknowledgements

Appendix A. Supplementary data

Supplementary data to this article can be found online at https://doi.org/10.1016/j.oregeorev.2024.106227.

References

Amaliksen, K.G., 1983. The geology of the Lykling Ophiolitic Complex, Bømlo. SW Norway. Unpubl. Cand. Real, Thesis, University of Bergen.

Amaliksen, K.G., Sturt, B.A., 1986. The Søre Lyklingholmen Formation: coarse sedimentary breccias related to submarine faulting in the Iapetus ocean. J. Geol. 94 (1), 109–120.

Andersen, T.B., Jansen, Ø.J., 1987. The Sunnhordland Batholith, W. Norway; regional setting and internal structure, with emphasis on the granitoid plutons. Norsk Geologisk Tidsskrift 67 (3), 159–183.

Andersen, T.B., Nielsen, P., Rykkelid, E., Sølna, H., 1991. Melt-enhanced deformation during emplacement of gabbro and granodiorite in the Sunnhordland Batholith, west Norway. Geol. Mag. 128 (3), 207–226.

Bark, G., Boyce, A.J., Fallick, A.E., Weihed, P., 2021. Fluid and metal sources in the Fäboliden hypozonal orogenic gold deposit, Sweden. Miner. Deposita 56, 425–440.

Bierlein, F.P., Crowe, D.E., 2000. Phanerozoic orogenic lode gold deposits. Rev. Econ. Geol. 13, 103–139.

Bodnar, R.J., 2003. Introduction to fluid inclusions. In: Samson, I., Anderson, A., Marshall, D. (Eds.), Fluid Inclusions: Analysis and Interpretation Mineralogical Association of Canada, pp. 1–8.

Botros, N.S., 2002. Metallogeny of gold in relation to the evolution of the Nubian Shield in Egypt. Ore Geol. Rev. 19 (3–4), 137–164.

Brekke, H., Furnes, H., Nordås, J., Hertogen, J., 1984. Lower Palaeozoic convergent plate margin volcanism on Bømlo, SW Norway, and its bearing on the tectonic environments of the Norwegian Caledonides. J. Geol. Soc. London 141 (6), 1015–1032.

Burgisser, A., Alletti, M., Scaillet, B., 2015. Simulating the behavior of volatiles belonging to the C–O–H–S system in silicate melts under magmatic conditions with the software D-Compress. Comput. Geosci. 79, 1–14.

Cathelineau, M., 1988. Cation site occupancy in chlorites and illites as a function of temperature. Clay Miner. 23 (4), 471–485.

Corfu, F., Andersen, T.B., Gasser, D., 2014. The Scandinavian Caledonides: main features, conceptual advances and critical questions. Geol. Soc. Lond. Spec. Publ. 390 (1), 9–43.

Doublier, M.P., Thébaud, N., Wingate, M.T., Romano, S.S., Kirkland, C.L., Gessner, K., Evans, N., 2014. Structure and timing of Neoarchean gold mineralization in the Southern Cross district (Yilgarn Craton, Western Australia) suggest leading role of late Low-Ca I-type granite intrusions. J. Struct. Geol. 67, 205–221.

Dubacq, B., Bickle, M.J., Evans, K.A., 2013. An activity model for phase equilibria in the H2O–CO2–NaCl system. Geochim. Cosmochim. Acta 110, 229–252.

Dunning, G.R., Pedersen, R.B., 1988. U/Pb ages of ophiolites and arc-related plutons of the Norwegian Caledonides: implications for the development of Iapetus. Contrib. Miner. Petrol. 98 (1), 13–23.

Fabricio-Silva, W., Frimmel, H.E., Emília Shutesky, M., Rosière, C.A., Massucatto, A.J., 2021. Temperature-controlled ore evolution in orogenic gold systems related to synchronous granitic magmatism: An example from the Iron Quadrangle Province, Brazil. Econ. Geol. 116 (4), 937–962.

Forsberg, F. R. (2021). Geochemical characteristics of the gold-bearing quartz veins in the Lykling area, Bømlo, SW Norway (Unpublished Master's thesis, The University of Bergen), 96 p.

Fossen, H., 2000. Extensional tectonics in the Caledonides: Synorogenic or postorogenic? Tectonics 19 (2), 213–224.

Fossen, H., Dunlap, W.J., 1998. Timing and kinematics of Caledonian thrusting and extensional collapse, southern Norway: evidence from 40Ar/39Ar thermochronology. J. Struct. Geol. 20 (6), 765–781.

Fossen, H., Hurich, C.A., 2005. The Hardangerfjord Shear Zone in SW Norway and the North Sea: a large-scale low-angle shear zone in the Caledonian crust. J. Geol. Soc. London 162 (4), 675–687.

Fossen, H., Khani, H.F., Faleide, J.I., Ksienzyk, A.K., Dunlap, W.J., 2017. Post-Caledonian extension in the West Norway–northern North Sea region: the role of structural inheritance. Geol. Soc. Lond. Spec. Publ. 439 (1), 465–486.

Fossen, H., Polonio, I., Bauck, M.S., Cavalcante, C., 2024. The North Sea rift basement records extensional collapse of the Caledonian orogen. Commun. Earth Environ. 5 (1), 206.

Furnes, H., Brekke, H., Nordås, J., Hertogen, J., 1986. Lower Palaeozoic convergent plate margin volcanism on Bømlo, southwest Norwegian Caledonides: geochemistry and petrogenesis. Geol. Mag. 123 (2), 123–142.

Gaboury, D., 2019. Parameters for the formation of orogenic gold deposits. Appl. Earth Sci. 128, 124–133.

Gee, D. G. (2015). Caledonides of Scandinavia, Greenland, and Svalbard. Reference Module in Earth Systems and Environmental Sciences, 2015.

Goldfarb, R. J., Baker, T., Dubé, B., Groves, D. I., Hart, C. J., & Gosselin, P. (2005). Distribution, character, and genesis of gold deposits in metamorphic terran. In Economic Geology 100th Anniversary Volume (eds. Hedenquist, J. W., Thompson, J. F. H., Goldfarb, R. J. & Richards, J. P.) 407–450 (Society of Economic Geologists, 2005).

Goldfarb, R.J., Pitcairn, I., 2023. Orogenic gold: is a genetic association with magmatism realistic? Miner. Deposita 58 (1), 5–35.

Goldfarb, R.J., Snee, L.W., Pickthorn, W.J., 1993. Orogenesis, high-T thermal events, and gold vein formation within metamorphic rocks of the Alaskan Cordillera. Mineral. Mag. 57 (388), 375–394.

Goldstein, R.H., 2001. Fluid inclusions in sedimentary and diagenetic systems. Lithos 55 (1–4), 159–193.

Grenne, T., Ihlen, P.M., Vokes, F.M., 1999. Scandinavian Caledonide metallogeny in a plate tectonic perspective. Miner. Deposita 34 (5), 422–471.

Groves, D.I., Goldfarb, R.J., Gebre-Mariam, M., Hagemann, S.G., Robert, F., 1998. Orogenic gold deposits: a proposed classification in the context of their crustal distribution and relationship to other gold deposit types. Ore Geol. Rev. 13 (1–5), 7–27.

Groves, D.I., Santosh, M., Deng, J., Wang, Q., Yang, L., Zhang, L., 2020. A holistic model for the origin of orogenic gold deposits and its implications for exploration. Miner. Deposita 55 (2), 275–292.

Hacker, B.R., Gans, P.B., 2005. Continental collisions and the creation of ultrahigh-pressure terranes: Petrology and thermochronology of nappes in the central Scandinavian Caledonides. Geol. Soc. Am. Bull. 117 (1–2), 117–134.

Hart, C.J., Goldfarb, R.J., Qiu, Y., Snee, L., Miller, L.D., Miller, M.L., 2002. Gold deposits of the northern margin of the North China Craton: multiple late Paleozoic-Mesozoic mineralizing events. Miner. Deposita 37, 326–351.

Hoefs, J., 2009. Stable Isotope Geochemistry. Springer-Verlag, Berlin, p. 388.

Johnson, J.W., Oelkers, E.H., Helgeson, H.C., 1992. SUPCRT92: A software package for calculating the standard molal thermodynamic properties of minerals, gases, aqueous species, and reactions from 1 to 5000 bar and 0 to 1000 C. Comput. Geosci. 18 (7), 899–947.

Kerr, M.J., Hanley, J.J., Kontak, D.J., Morrison, G.G., Petrus, J., Fayek, M., Zajacz, Z., 2018. Evidence of upgrading of gold tenor in an orogenic quartz-carbonate vein system by late magmatic-hydrothermal fluids at the Madrid Deposit, Hope Bay Greenstone Belt, Nunavut, Canada. Geochim. Cosmochim. Acta 241, 180–218.

Ledru, P., 1980. Evolution structurale et magmatique du complexe plutonique de Karmoy (sud-ouest des Calidonides norvegiennes). Sot. Geol. Mitt&al. Bretagne Bull., Ser. C 12 (2), 106.

Melezhik, V.A., Ihlen, P.M., Kuznetsov, A.B., Gjelle, S., Solli, A., Gorokhov, I.M., Bjerkgård, T., 2015. Pre-Sturtian (800–730 Ma) depositional age of carbonates in sedimentary sequences hosting stratiform iron ores in the Uppermost Allochthon of the Norwegian Caledonides: A chemostratigraphic approach. Precambr. Res. 261, 272–299.

Nordås, J., Amaliksen, K.G., Brekke, H., Suthern, R., Furnes, H., Sturt, B.A., Gee, D.G., 1985. Lithostratigraphy and petrochemistry of Caledonian rocks on Bømlo. In: SW Norway. the Caledonide Orogen—Scandinavia and Related Areas. John Wiley & Sons Ltd, New York, pp. 679–692.

Patten, C.G.C., Pitcairn, I.K., Molnár, F., Kolb, J., Beaudoin, G., Guilmette, C., Peillod, A., 2020. Gold mobilization during metamorphic devolatilization of Archean and Paleoproterozoic metavolcanic rocks. Geology 48 (11), 1110–1114.

Paulsson, O., Andréasson, P.G., 2002. Attempted break-up of Rodinia at 850 Ma: geochronological evidence from the Seve-Kalak Superterrane, Scandinavian Caledonides. J. Geol. Soc. London 159 (6), 751–761.

Pedersen, R.B., Furnes, H., 1991. Geology, magmatic affinity and geotectonic environment of some Caledonian ophiolites in Norway. J. Geodyn. 13 (2–4), 183–203.

Pedersen, R.B., Hertogen, J., 1990. Magmatic evolution of the Karmøy Ophiolite Complex, SW Norway: relationships between MORB-IAT-boninitic-calc-alkaline and alkaline magmatism. Contrib. Miner. Petrol. 104 (3), 277–293.

Pedersen, R.B., Bruton, D.L., Furnes, H., 1992. Ordovician faunas, island arcs and ophiolites in the Scandinavian Caledonides. Terra Nova 4 (2), 217–222.

Pedersen, R.B., Dunning, G.R., 1997. Evolution of arc crust and relations between contrasting sources: U-Pb (age), Nd and Sr isotope systematics of the ophiolitic terrane of SW Norway. Contrib. Miner. Petrol. 128 (1), 1–15.

Phillips, G.N., Powell, R., 2010. Formation of gold deposits: a metamorphic devolatilization model. J. Metam. Geol. 28 (6), 689–718.

Révész, K.M., Landwehr, J.M., 2002. Delta13C and delta18O isotopic composition of CaCO3 measured by continuous flow isotope ratio mass spectrometry: statistical evaluation and verification by application to Devils Hole core DH-11 calcite. Rapid Commun. Mass Spectrom. 16 (22), 2102–2114.

Ridley, J., Diamond, L., 2000. Fluid chemistry of orogenic lode gold deposits and implications for genetic models. Soc. Econ. Geol. Rev. 13, 141–162.

Roberts, D., 2003. The Scandinavian Caledonides: event chronology, palaeogeographic settings and likely modern analogues. Tectonophysics 365 (1–4), 283–299.

Rosenbaum, J., Sheppard, S.M.F., 1986. An isotopic study of siderites, dolomites and ankerites at high temperatures. Geochim. Cosmochim. Acta 50 (6), 1147–1150.

Saltvedt, S., 2021. The formation of the ophiolitic terrane of SW Norway-relationships between immature island arc volcanic sequences and trondhjemitic complexes on Bømlo. The University of Bergen), p. 102. Unpublished Master's thesis.

Savard, D., Bouchard-Boivin, B., Barnes, S.J., Garbe-Schönberg, D., 2018. UQAC-FeS: A new series of base metal sulfide quality control reference material for LA-ICP-MS analysis. Proceedings of the 10th International Conference on the Analysis of Geological and Environmental Materials, Sydney, Australia.

Seward, T.M., Williams-Jones, A.E., Migdisov, A.A., 2014. 13.2–The chemistry of metal transport and deposition by ore-forming hydrothermal fluids. Treat. Geochem. 13, 29–57.

Sharma, S.D., Patil, D.J., Gopalan, K., 2002. Temperature dependence of oxygen isotope fractionation of CO2 from magnesite-phosphoric acid reaction. Geochim. Cosmochim. Acta 66 (4), 589–593.

Sibson, R.H., 2004. Controls on maximum fluid overpressure defining conditions for mesozonal mineralisation. J. Struct. Geol. 26 (6–7), 1127–1136.

Sibson, R.H., 2020. Preparation zones for large crustal earthquakes consequent on fault-valve action. Earth Planets Space 72, 1–20.

Sibson, R.H., Scott, J., 1998. Stress/fault controls on the containment and release of overpressured fluids: Examples from gold-quartz vein systems in Juneau, Alaska; Victoria, Australia and Otago. New Zealand. Ore Geology Reviews 13 (1–5), 293–306.

Sibson, R.H., Robert, F., Poulsen, K.H., 1988. High-angle reverse faults, fluid-pressure cycling, and mesothermal gold-quartz deposits. Geology 16 (6), 551–555.

Slagstad, T., Davidsen, B., Daly, J.S., 2011. Age and composition of crystalline basement rocks on the Norwegian continental margin: offshore extension and continuity of the Caledonian-Appalachian orogenic belt. J. Geol. Soc. London 168 (5), 1167–1185.

Slagstad, T., Kirkland, C.L., 2018. Timing of collision initiation and location of the Scandian orogenic suture in the Scandinavian Caledonides. Terra Nova 30 (3), 179–188.

Spangenberg, J.E., Saintilan, N.J., Strmić Palinkaš, S., 2022. Safe, accurate, and precise sulfur isotope analyses of arsenides, sulfarsenides, and arsenic and mercury sulfides by conversion to barium sulfate before EA/IRMS. Anal. Bioanal. Chem. 414, 2163–2279.

Stakes, D.S., O'neil, J.R., 1982. Mineralogy and stable isotope geochemistry of hydrothermally altered oceanic rocks. Earth Planet. Sci. Lett. 57 (2), 285–304.

Steele-MacInnis, M., 2018. Fluid inclusions in the system H2O-NaCl-CO2: An algorithm to determine composition, density and isochore. Chem. Geol. 498, 31–44.

Steele-MacInnis, M., Lecumberri-Sanchez, P., Bodnar, R.J., 2012. HokieFlincs_H2O-NaCl: A Microsoft Excel spreadsheet for interpreting microthermometric data from fluid inclusions based on the PVTX properties of H2O–NaCl. Comput. Geosci. 49, 334–337.

Stepanov, A.S., 2021. A review of the geochemical changes occurring during metamorphic devolatilization of metasedimentary rocks. Chem. Geol. 568, 120080.

Stephens, M.B., 2020. Upper and uppermost thrust sheets in the Caledonide orogen, Sweden: outboard oceanic and exotic continental terranes. Geol. Soc. Lond. Mem. 50 (1), 549–575.

Strmić Palinkaš, S., Peltekovski, Z., Tasev, G., Serafimovski, T., Šmajgl, D., Rajič, K., Spangenberg, J.E., Neufeld, K., Palinkaš, L., 2018. The role of magmatic and hydrothermal fluids in the formation of the Sasa Pb-Zn-Ag skarn deposit, Republic of Macedonia. Geosciences 8 (12), 444.

Strmić Palinkaš, S., Fjellet, T., Stubseid, H.H., Liu, X., Spangenberg, J.E., Čobić, A., Pedersen, R.B., 2024. Trace-Element and Sulfur Isotope Signatures of Volcanogenic Massive Sulfide (VMS) Mineralization: A Case Study from the Sunnhordland Area in SW Norway. Minerals 14 (4), 384.

Tavares, Nassif M., Monecke, T., Reynolds, T.J., Kuiper, Y.D., Goldfarb, R.J., Piazolo, S., Lowers, H.A., 2022. Formation of orogenic gold deposits by progressive movement of a fault-fracture mesh through the upper crustal brittle-ductile transition zone. Sci. Rep. 12 (1), 17379.

Ulrich, T., Kamber, B. S., Jugo, P. J., and Tinkham, D. K. (2009). Imaging element-distribution patterns in minerals by laser ablation - Inductively coupled plasma - Mass spectrometry (LA-ICP-MS): Canadian Mineralogist, 47, 1001–1012.

Vanko, D.A., Bodnar, R.J., Sterner, S.M., 1988. Synthetic fluid inclusions: VIII. Vapor saturated halite solubility in part of the system NaCl-CaCl2-H2O, with application to fluid inclusions from oceanic hydrothermal systems. Geochim. Cosmochim. Acta 52 (10), 2451–2456.

Veizer, J., Hoefs, J., 1976. The nature of O18/O16 and C13/C12 secular trends in sedimentary carbonate rocks. Geochim. Cosmochim. Acta 40 (11), 1387–1395.

Vry, J., Powell, R., Golden, K.M., Petersen, K., 2010. The role of exhumation in metamorphic dehydration and fluid production. Nat. Geosci. 3 (1), 31–35.

White, A.J., Waters, D.J., Robb, L.J., 2015. Exhumation-driven devolatilization as a fluid source for orogenic gold mineralization at the Damang deposit. Ghana. Economic Geology 110 (4), 1009–1025.

Wilson, S.A., Ridley, W.I., Koenig, A.E., 2002. Development of sulfide calibration standards for the laser ablation inductively-coupled plasma mass spectrometry technique. J. Anal. At. Spectrom 17, 406–409.

Woodhead, J.D., Hellstrom, J., Hergt, J.M., Greig, A., Maas, R., 2007. Isotopic and elemental imaging of geological materials by laser ablation inductively coupled plasma-mass spectrometry. Geostand. Geoanal. Res. 31, 331–343.

Wulff, P., & Stendal, H. (1995). Gold in Sunnhordland, the Caledonides of southwestern Norway. Gold mineralization in the Nordic countries and Greenland. Extended abstracts and fieldtrip guide, Grùnl Geol Unders Open File Series, 95(10), 116-119.

Zoheir, B., 2011. Transpressional zones in ophiolitic mélange terranes: potential exploration targets for gold in the South Eastern Desert, Egypt. J. Geochem. Explorat. 111 (1–2), 23–38.

Zoheir, B., Emam, A., Abd El-Wahed, M., Soliman, N., 2019a. Gold endowment in the evolution of the Allaqi-Heiani suture, Egypt: A synthesis of geological, structural, and space-borne imagery data. Ore Geol. Rev. 110, 102938.

Zoheir, B.A., Johnson, P.R., Goldfarb, R.J., Klemm, D.D., 2019c. Orogenic gold in the Egyptian Eastern Desert: Widespread gold mineralization in the late stages of Neoproterozoic orogeny. Gondw. Res. 75, 184–217.

Zoheir, B., Steele-MacInnis, M., Garbe-Schönberg, D., 2019b. Orogenic gold formation in an evolving, decompressing hydrothermal system: Genesis of the Samut gold deposit, Eastern Desert, Egypt. Ore Geol. Rev. 105, 236–257.